

A SHALLOW SEISMIC REFRACTION SURVEY OVER A  
LATE QUATERNARY FAULT SCARP WEST OF THE  
SANTA RITA MOUNTAINS, ARIZONA

by

James Thomas Rutledge

---

A Thesis Submitted to the Faculty of the  
DEPARTMENT OF GEOSCIENCES  
In Partial Fulfillment of the Requirements  
For the Degree of  
MASTER OF SCIENCE  
In the Graduate College  
THE UNIVERSITY OF ARIZONA

1 9 8 4

Call No.	BINDING INSTRUCTIONS	INTERLIBRARY INSTRUCTIONS
E9791 1984 371	Author: Rutledge, J. Title: COLOR: M.S.	Dept. _____ RUSH _____ PERMABIND _____ PAMPHLET _____ GIFT _____ POCKET FOR MAP _____ COVERS _____ Front _____ Both _____ REFERENCE _____ Other _____
Special Instructions - Bindery or Repair	11/22/85	L-379 L-379
Spe		

STATEMENT BY AUTHOR

This thesis has been submitted in partial fulfillment of requirements for an advanced degree at The University of Arizona and is deposited in the University Library to be made available to borrowers under rules of the Library.

Brief quotations from this thesis are allowable without special permission, provided that accurate acknowledgment of source is made. Requests for permission for extended quotation from or reproduction of this manuscript in whole or in part may be granted by the head of the major department or the Dean of the Graduate College when in his or her judgment the proposed use of the material is in the interests of scholarship. In all other instances, however, permission must be obtained from the author.

SIGNED:

James T. Rutledge

APPROVAL BY THESIS DIRECTOR

This thesis has been approved on the date shown below:

Randall M. Richardson

R. M. RICHARDSON

Associate Professor of Geosciences

27 August 1984  
Date

## ACKNOWLEDGMENTS

I would like to recognize the many people who contributed to the completion of this study. My foremost appreciation goes to Dr. Randy Richardson, my major advisor, for his careful review of the text, his honest advice, and his aid in the field. I also thank my other advisors, Dr. Terry Wallace and Dr. John Sumner for their review of the text and especially Terry's help in seismic interpretation.

I thank all those who contributed to the many man-hours of field work required for data acquisition. The list is too long to enumerate all, but I would like to recognize those fellow students who were repeatedly available for assistance: Terri McDonald, Dave Newton, Dave Senske, Dave Kistner, Rik Lantz, and Lynn Reding. I especially thank Dr. Marc Sbar for his help in planning the survey and his involvement of the 1983 Geoscience 413b Geophysics Field Studies course in this study.

The explosives used as a seismic source, blasting caps and Iremite were donated by the Apache Powder Company and Ireco Chemicals respectively.

An A.A.P.G. Grant-In-Aid was awarded for this study to defray expenses of transportation, field equipment, and data processing.

## TABLE OF CONTENTS

	Page
LIST OF ILLUSTRATIONS . . . . .	vi
LIST OF TABLES . . . . .	viii
ABSTRACT . . . . .	ix
 CHAPTER	
1. INTRODUCTION . . . . .	1
Statement of the Problem . . . . .	3
Purpose and Scope . . . . .	3
Location and Previous Work . . . . .	5
2. DATA ACQUISITION AND REDUCTION . . . . .	11
3. PRELIMINARY INTERPRETATION . . . . .	15
Picking Arrival Times . . . . .	15
Evidence for a Near-surface Velocity Inversion . . . . .	16
Assigning Arrival Times to Refractors . . . . .	19
4. THE GENERALIZED RECIPROCAL METHOD OF SEISMIC REFRACTION INTERPRETATION . . . . .	26
The Conventional Time-depth . . . . .	27
The Generalized Time-depth and Velocity Analysis Functions . . . . .	33
Determining the Average Velocity Above a Refractor . . . . .	41
Determination of the Bedrock Surface using the GRM . . . . .	46
Determining Optimum XY-values . . . . .	47
Removal of Near-surface Anomaly . . . . .	54
Conversion of Time-depths to Depth Values . . . . .	60
5. MAPPING SHALLOW ALLUVIAL SURFACES . . . . .	64

TABLE OF CONTENTS -- Continued

	Page
Determining an Average Overburden Velocity for the Base of the LVL . . . .	64
Determination of the Base of the LVL using the Delay Time Method of Refractor Mapping . . . . .	68
A Qualitative Discussion on the Deep Alluvial Refractor . . . . .	77
6. INTERPRETATION OF THE STRIKE PROFILES . . . .	80
7. GEOLOGIC INTERPRETATION . . . . .	86
Geologic Features . . . . .	86
Implications for Faulting History . . . .	87
Conclusions . . . . .	89
REFERENCES . . . . .	91

## LIST OF ILLUSTRATIONS

Figure		Page
1.	Location of the refraction survey . . . . .	6
2.	Detailed location and layout of refraction survey . . . . .	9
3.	Dip line refraction profile layout . . . . .	12
4.	Shot record of shotpoint 4, spread 4 . . . . .	17
5.	Dip line travel time curves . . . . .	20
6.	Shot records of shotpoints 1 and 2 over spread 4 . . . . .	23
7.	Ray paths of conventional time-depth . . . . .	28
8.	Time-depth relationship to depth . . . . .	30
9.	Ray paths in calculation of generalized time-depth . . . . .	34
10.	Velocity analysis curves derived from arrival times of the bedrock refractor . . . . .	38
11.	Time-depths derived from arrival times of the bedrock refractor . . . . .	39
12.	Symbols used in definition of the average velocity above nth horizon . . . . .	44
13.	Bedrock velocity analysis curves at expanded time scale . . . . .	48
14.	Bedrock time-depths at expanded time scale . . . . .	53
15.	Schematic diagram of optimized ray paths with travel time data of the composite arrival time curves . . . . .	56
16.	Bedrock time-depths after removal of shallow anomaly . . . . .	58

LIST OF ILLUSTRATIONS -- Continued

Figure		Page
17.	Bedrock velocity analysis curves after removal of shallow anomaly . . . . .	59
18.	Depth section of the bedrock refractor . . . . .	63
19.	Velocity analysis curves for the base of the LVL . . . . .	65
20.	Time-depths for the base of the LVL . . . . .	66
21.	Arrival time data from the base of the LVL of shots 2a, 3 and supplementary shots 6, 7, 9, 11, 14, and 18 . . . . .	69
22.	Intercept curves . . . . .	71
23.	Comparison of fit of delay times . . . . .	75
24.	Final dip line depth profile . . . . .	78
25.	Bedrock arrival time curves of strike profiles . . . . .	81
26.	Bedrock depth sections derived from strike profiles . . . . .	83

LIST OF TABLES

Table		Page
1.	Bedrock refractor velocities $V_r'$ , and optimum XY-values . . . . .	50
2.	Average time-depth $t_G$ , average overburden velocity $\bar{V}$ , and depth conversion factor for the three segments of the bedrock refractor .	61
3.	GRM parameters for the shallow alluvial horizon . . . . .	67
4.	Comparison of depth values and refractor velocity from strike and dip profiles at their respective points of intersection . . .	84

## ABSTRACT

A 3300 ft seismic refraction profile was shot perpendicular to a fault scarp west of the Santa Rita Mountains south of Tucson, Arizona. Previous geomorphic work along the Santa Rita Mountains indicated two fault-displacement events during the past 200,000 years. The present seismic study was undertaken to infer faulting history by delineating subsurface structure.

A suballuvial bedrock pediment surface and a shallower alluvial horizon were mapped in profile using the generalized reciprocal method of refraction interpretation (Palmer, 1980). The bedrock shows a minimum normal offset of 50 ft at an approximate depth of 500 ft. The alluvial horizon shows 10 ft of normal offset at an approximate depth of 70 ft. These offsets indicate 40 to 65 ft of fault displacement occurred between burial of the bedrock pediment surface and deposition of the shallow alluvial horizon.

## CHAPTER 1

### INTRODUCTION

The present day topography of the Basin and Range province of southeastern Arizona is largely the result of regional extensional block faulting that began 13 to 10 m.y. ago (Scarborough and Peirce, 1978; Eberly and Stanley, 1978; Shafiqullah, 1978). The area is structurally dominated by high-angle normal faults bounding isolated mountain ranges with intermontane basins. The resultant basins are depositional sites of detrital sediments derived from the adjacent mountains. Two basin studies in southeastern Arizona (the Sonoita Creek and Canada del Oro basins) indicate cessation of the main phase of Basin-Range deformation between 6 and 3 m.y. ago (McFadden, 1978; Menges, 1981; Menges and McFadden, 1981). These dates are inferred from the occurrence of faulted syntectonic Miocene sediments buried by unfaulted basin fill of latest Miocene to Pliocene age. Subsequent basin sediments extend generally undisturbed over the location of basin-bounding faults as sited in outcrop or projected to the surface from gravity data locations. Further evidence for the waning and termination of large vertical displacement is the development of extensive bedrock pediments between the

present day mountain fronts and the range-bounding faults of these and other basins of southeastern Arizona.

Although there is clear evidence for the quiescence of Basin-Range tectonic activity since latest Miocene to early Pliocene in southeastern Arizona, some activity has continued or recurred. This more recent tectonism is manifested by the presence of young normal faults offsetting piedmont surfaces of the late Pliocene to late Pleistocene (Morrison, Menges and Lephley, 1981; Drewes, 1973; Pearthree and Calvo, 1982). These scarps generally trend parallel to Basin-Range structures. Most of the recent faulting of this area occurred in a belt near the southern border of Arizona and New Mexico during the Quaternary (Pearthree, Menges and Calvo, 1982). The most detailed study (Pearthree and Calvo, 1982) to date of Quaternary faults in southeastern Arizona was done adjacent to this belt along the western piedmont of the Santa Rita Mountains. Pearthree, Menges and Calvo (1982) have identified several other scarps peripheral to the belt in southeastern Arizona, New Mexico and Sonora, Mexico. Overall, Quaternary faulting occurs along approximately one-third of the mountain fronts of the region. Determination of faulting recurrence intervals, where possible, consistently indicates a period on the order of 100,000 years.

### Statement of Problem

All the mountain fronts associated with the recent faulting in southeastern Arizona show some degree of pedimentation. The presence of surface ruptures over suballuvial bedrock pediments, trending parallel to Basin-Range structures, has led to the implication that the young faults are the result of Quaternary reactivation along Basin-Range faults. A 4 to 6 m.y. period of tectonic quiescence has been estimated from a tectonic landform analysis along the Santa Rita Mountain front. Renewed movement has been restricted to the last several hundred thousand years as one or two rupture events based on geomorphic analysis of scarps and the relative offsets of dated surfaces (Morrison and others, 1981; Pearthree and Calvo, 1982). Because these restrictions are based on the preservation of resultant land forms, they become more limited in resolution with age. Furthermore, the occurrence of these recent rupture events along pre-existing structures can only be inferred from surficial data. If pre-Quaternary movement occurred along these faults, evidence for reactivation should be preserved in the subsurface.

### Purpose and Scope

The purpose of this study is to examine a Quaternary fault at depth. Specifically, the objective is to infer

faulting history from subsurface structure by mapping in profile, across strike, the suballuvial bedrock pediment surface and any shallower alluvial horizons using seismic refraction methods.

Seismic refraction prospecting techniques are very effective for mapping extensive horizons which bound a relatively high seismic velocity contrast such as bedrock surfaces. If faulting has occurred prior to the constraining dates established at the surface, offset observed in the suballuvial bedrock pediment will be greater than offsets observed at the surface. Further, if overlying alluvial horizons can be delineated, the relative offsets of subsequent horizons would indicate relative timing of additional movement recorded.

A detailed, in-line seismic refraction survey was shot across strike of an identified Quaternary surface rupture west of the Santa Rita Mountains about 20 miles southeast of Tucson, Arizona. This paper demonstrates, in one example, the use of shallow seismic refraction data in revealing faulting history and fault geometry that is not evident from surficial data. The results may have implications for the neotectonic history of southeastern Arizona.

### Location and Previous Work

The approximate location of the refraction profile is 2.5 miles west of Sycamore Canyon, and is shown in Figure 1. The map of Figure 1 shows the Quaternary fault scarps identified by Drewes (1973) and mapped in detail by Pearthree and Calvo (1982) along 22 miles of the western piedmont of the Santa Rita Mountains. Pearthree and Calvo further sited the scarps extending another 14 miles southward (shown with question marks). The 36-mile segmented occurrence of fault scarps trends N-S to N45E, subparallel to the topographic mountain front, but located approximately 0.5 to 4 miles basinward. Scarp heights ranged from 3 to nearly 25 ft. The work of Pearthree and Calvo is the most detailed study to date of Quaternary faulting in this area and, for that matter, in all of southeastern Arizona. What follows is a brief summary of their work.

Detailed geomorphic analysis of scarps offsetting Quaternary alluvium on, and in the vicinities of, Madera Canyon Fan and Sycamore Canyon Fan (Figure 1) indicate two late Quaternary surface rupture events, the first dated about 200,000 years B.P. and the latest about 100,000 years B.P. Estimates of ages were obtained from offset relationships of dated surfaces and from morphological analysis of fault scarps. With a chronosequence of alluvial surfaces the most recent surface rupture was constrained to have occurred prior

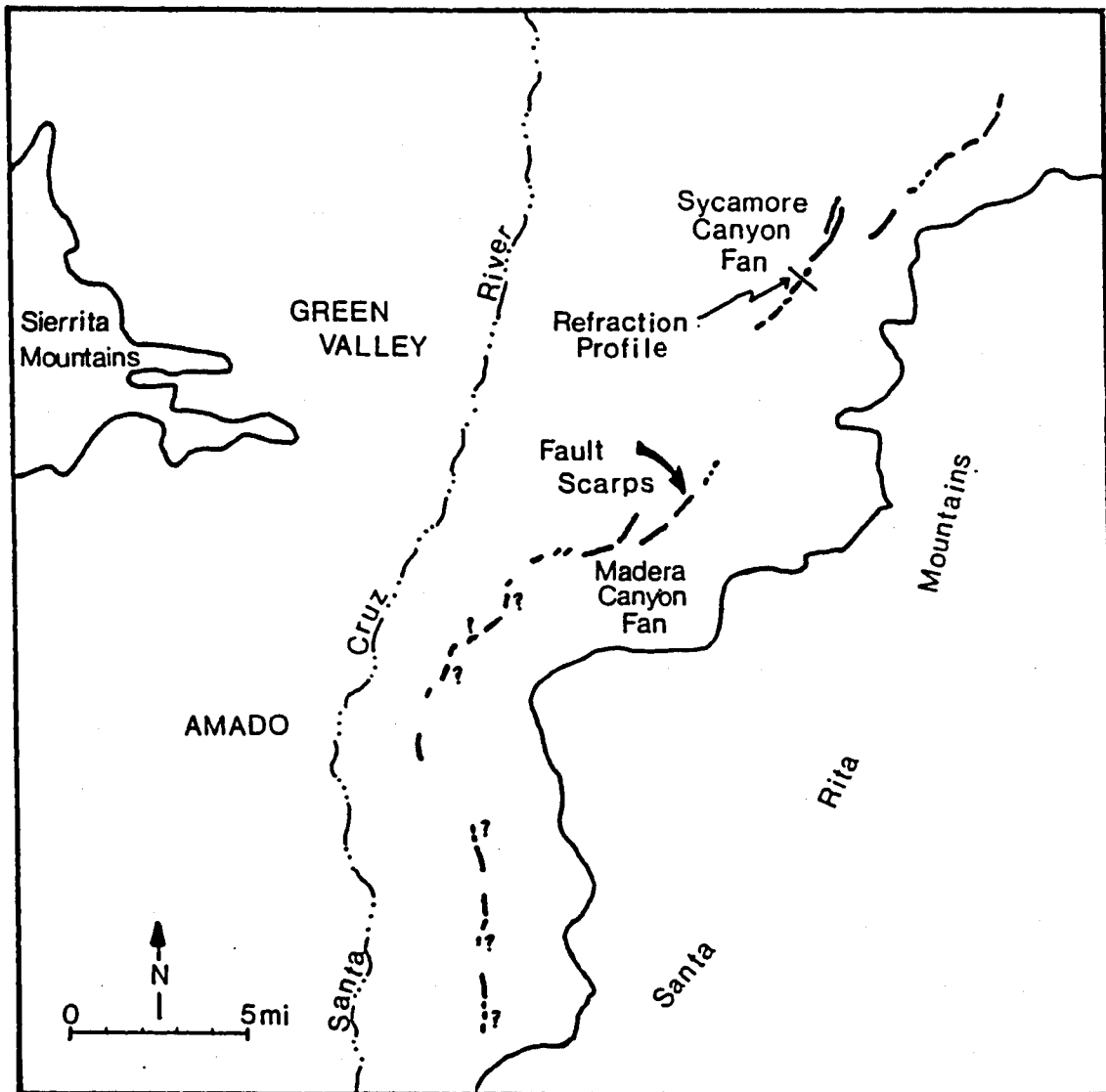


Figure 1. Location of the refraction survey.

to the oldest surface not offset and after the youngest surface cut by faulting. The two episodes of movement were inferred from a difference in scarp height with age of surfaces offset. Scarp heights on surfaces of early and late mid-Pleistocene age are significantly greater than scarp heights on late Pleistocene surfaces. Therefore it is implied that surfaces of late mid-Pleistocene and older have recorded two surface rupture events and surfaces of late Pleistocene only one. Stratigraphic relationships in a trench excavation near the Madera Canyon Fan also indicated two episodes of faulting and put better constraints on the timing of the events. The earlier faulting event is constrained to during or since the mid-Pleistocene from lack of increase in scarp height between surfaces of early to mid-Pleistocene. No earlier faulting is evident from the surface data.

A previous geophysical study (Stevenson and others, 1981) employing numerous potential field methods and shallow seismic refraction data was conducted in the Madera Canyon Fan area. Partly as an experiment for evaluating the effectiveness of various geophysical techniques in measuring the depth to the water table in this area, the study also sought to measure the depth to the suballuvial bedrock and subsurface fault displacement. Subsurface offset was inferred from anomalies detected by the various potential methods. Seismic refraction profiles shot across a scarp failed to

reveal the bedrock surface or to resolve offset in the subsurface alluvial horizons. The refraction data indicated the existence of alluvium to a depth of at least 250 ft and verified that the non-unique models fitted to the gravity and magnetic data profiles were not valid.

The map of Figure 2 shows in detail the location of the dip line refraction profile shot for this study along the road leading to Helvetia. The 3300 foot long profile was centered on the projected location of the fault. No surface expression exists along the dip profile because Holocene deposition has subsequently buried the scarp (Pearthree, personal communication, 1984).

Two refraction profiles, approximately 2000 ft in length, were shot along strike on each side of the scarp as a field exercise for the University of Arizona, 1982, Geoscience 413b Geophysics Field Studies course (Figure 2). The initial interpretation of this data (unpublished) was incorrect due to failure to recognize a near-surface velocity inversion (see Chapter 3) and poor spatial resolution of receivers resulting in a deeper layer on the upthrown block occurring as a hidden layer. Field procedures used in shooting the dip profile provided data appropriate for a more advanced interpretational method (Chapter 4) which overcomes these problems. The strike profile data was then

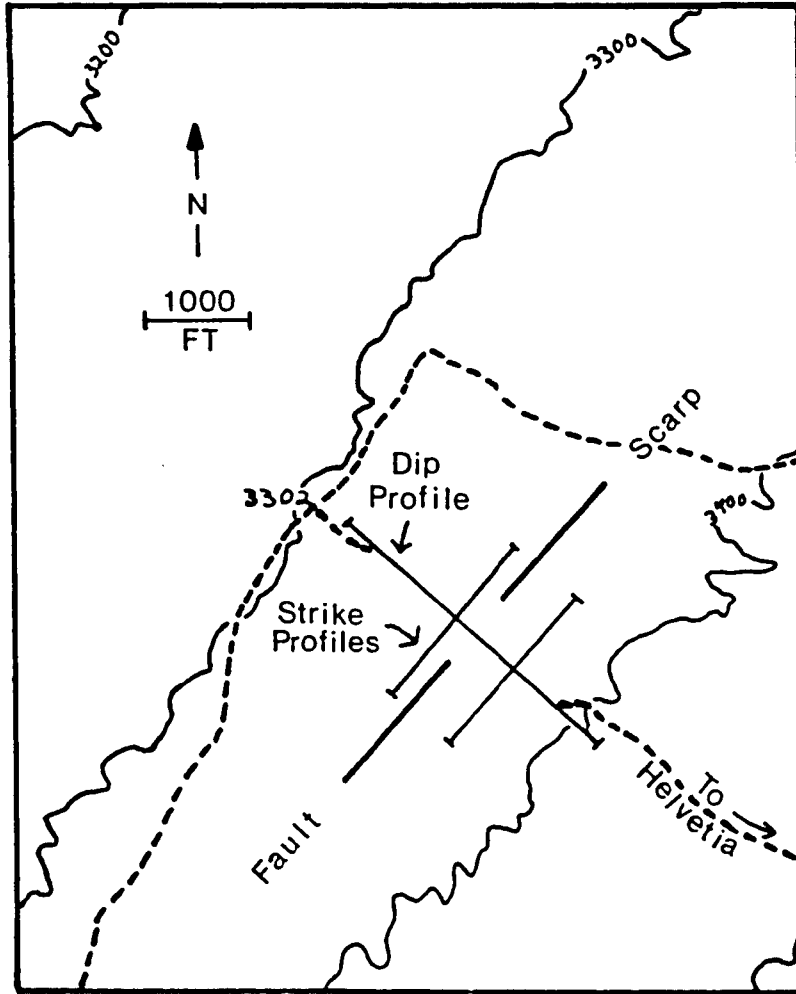


Figure 2. Detailed location and layout of refraction survey.

incorporated into the interpretation. It was also of aid in planning the dip profile layout.

## CHAPTER 2

### DATA ACQUISITION AND REDUCTION

The refraction profile layout was designed to efficiently collect a large amount of data for determining both shallow and relatively deep structure. The layout is illustrated in Figure 3. All shotpoints and geophones station locations are given in feet with respect to shotpoint 1 at station 0. The total 3300 foot spread of 45 geophone stations is a composite of four adjacent 12 station spreads with each adjacent spread sharing a common geophone location. Geophone station intervals are 90 ft for the two end spreads 1 and 4. A 60 ft interval was used for the two center spreads, 2 and 3, for greater spatial resolution over the fault zone. A Brunton compass and tape-measure were used for surveying the line layout. Elevations were then assigned to each geophone station and shotpoint by tying in their relative elevations, determined with a self-leveling transit, to the spot elevation of 3302 ft at the nearby road intersection (Figure 2).

Data was collected using the Nimbus ES-1200 twelve channel signal enhancement seismograph and the Nimbus G-724S digital tape recorder. Iremite 80, a chemical explosive, was detonated in shallow holes to provide an energy source.

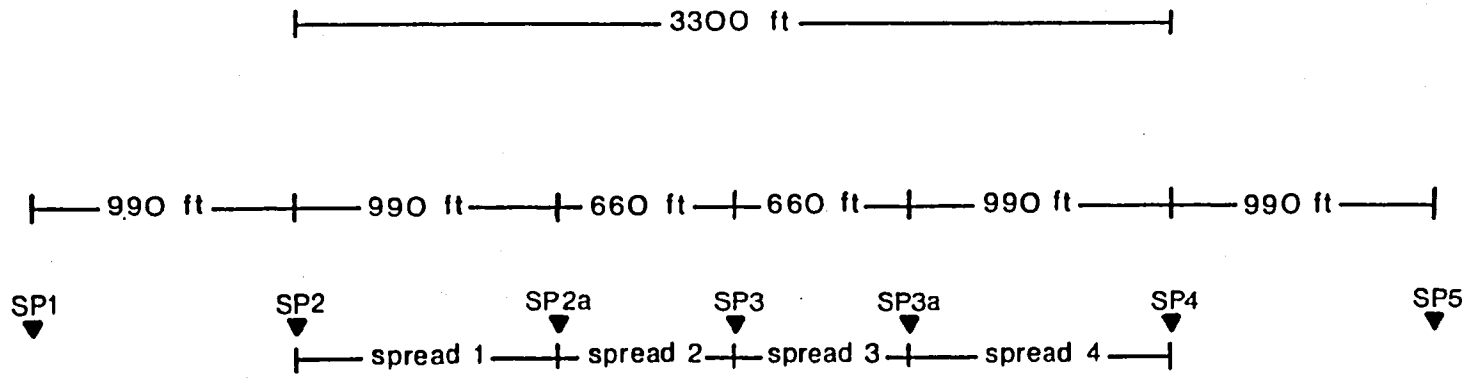


Figure 3. Dip line refraction profile layout.

Arrival times were recorded over all four spreads for shotpoints 1, 2, 3, 4, and 5. This required each of these shotpoints to be shot 4 times, once for each spread location. Shotpoints 2 and 4 reciprocate the entire 3300 ft profile. Shotpoint 3 is a split shot for the whole profile length; this was done to reciprocate the near offset geophone stations of shots 2 and 4 in order to map shallow horizons on each side of the fault scarp. Shotpoints 2a and 3a reciprocate the 60 ft geophone interval spreads 2 and 3 for shallow detail across the fault. The off-end shotpoints 1 and 5, located 990 ft on each end of the 3300 ft profile, were used to facilitate interpretation of deeper structure (see Chapter 3).

The most efficient shooting procedure was to lay out a geophone spread, shoot it from each shotpoint location, then move the geophone spread to an adjacent location and reshoot each shotpoint for that spread. Adjacent geophone spreads had one common geophone station in order to check the timing of subsequent shots from a particular shotpoint. The Iremite was placed in holes approximately 4 ft deep and 8 to 12 inches wide. The hole was then tamped with water and soil to insure good coupling with the earth. Charge sizes ranged from 0.125 to 1.75 pounds depending on the offsets of shotpoint and receivers. A zero-delay, seismic-grade blasting cap was placed within the Iremite for detonation. The blasting cap itself was detonated by an electrical potential

built up in an electronic blasting machine. A twin lead connected from the blaster to the seismograph simultaneously turns the recorder on with detonation of the explosive. Data digitally recorded by the Nimbus ES-1200 seismograph can be played back and displayed on light-sensitive photographic paper. This was done in the field as a data quality check before recording the data on magnetic tape with the Nimbus G-724S digital tape recorder.

The seismic data recorded on the field tapes is in a hexadecimal format and unsorted. After returning from the field, the field tapes are played back and the data temporarily stored on the disk storage space of the University of Arizona DEC-10 computer. Using an editing program, the data is then sorted by separating the individual shot records and the individual channels of each shot. The data is next converted to decimal using the program CONVRT (Sene, 1983). This program also assigns specified header information to each shot record to be used for labeling and other processing routines. The individual shot records, as output files of program CONVRT, are permanently stored on 9-track tape. Finally, the shot records are plotted on a Calcomp plotter using the program SPLOT (Sene, 1983). These plots are used for the preliminary interpretation of the seismic refraction data.

## CHAPTER 3

### PRELIMINARY INTERPRETATION

The preliminary interpretation of the seismic refraction data includes picking refraction arrival times, recognizing arrival time anomalies from the shot records and assigning arrival times to refractors. This is a very important phase of the interpretation because all further manipulation of the data is dependent on the judgment exercised here and the accuracy achieved.

#### Picking Arrival Times

For this study, only first break arrival times were used. Later refraction and reflection events were not recognized on the shot records. The arrival times assigned to each offset location correspond to the onset of the first break wavelet for that trace. For relatively noiseless traces this was accurately determined to  $\pm 0.5$  milliseconds (msec). The onset of first breaks may be somewhat masked on noisier traces or on far offset traces where the frequency content of the first arrivals is lower. The peaks of first breaks, on the other hand, could nearly always be well determined. Frequency of first event pulses varied little over a few geophone intervals at offsets greater than several hundred

feet. If the peaks of first breaks showed a good linear trend over a few geophone intervals, then the arrival times of noisier traces could be determined by translating the peak-to-peak line segment to the onset of the pulse of the cleanest trace of that group. First break irregularities from trace to trace were preserved as much as possible when picking times for noisy channels or low-amplitude events by individual comparison of the wavelet character with nearby traces with better-defined breaks. The accuracy of picks for the noisier traces ranged approximately from  $\pm 1$  msec to  $\pm 2$  msec.

#### Evidence for a Near-surface Velocity Inversion

Careful inspection of the shot records was critical in recognizing the cause of a near-surface arrival time anomaly. On all the near-offset shot records, skips or discontinuities of first arrivals were observed (Figure 4). Other case studies (Domzalski, 1956, pp. 153-155; Press and Dobrin, 1956) have shown that this phenoma is due to a near-surface velocity inversion. A head wave propagating along a thin, high-velocity layer capping a thicker, low-velocity layer is attenuated due to leakage of energy downward into the lower-speed medium. Leakage of the head wave decreases with increasing frequency so that the thin, high-speed layer acts as a high pass filter in the horizontal direction (Press

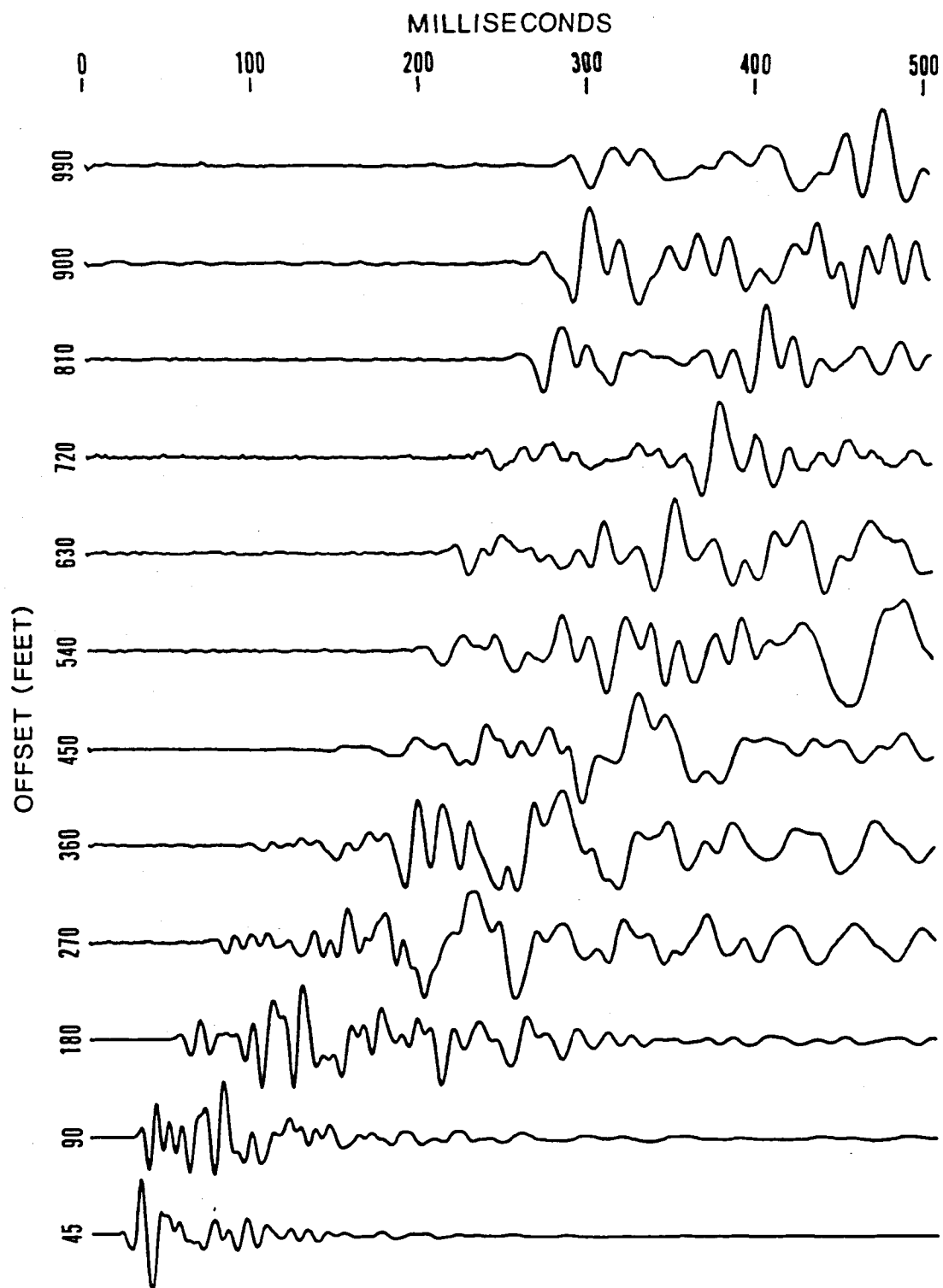


Figure 4. Shot record of shotpoint 4, spread 4.

and Ewing, 1948). First breaks from the thin, high-speed layer then should decrease in amplitude with offset and increase in frequency. With their rapid attenuation, these breaks become undetectable and the next first breaks observed come from the base of the low-velocity layer (LVL) resulting in a discontinuity or skip on the shot records. This phenomena is well illustrated on the near-offset shot record of shotpoint 4 (Figure 4). The near-offset traces from 45 to 360 ft show first arrival wavelets which decrease in amplitude and increase in frequency with increasing offset. At 450 ft, the first break from the thin, high-speed layer is undetectable. Subsequent offset traces show later first breaks from the base of the LVL.

A well developed caliche layer observed in several washes of the study area is probably the cause of the shallow velocity inversion. The caliche, with a relatively high velocity of approximately 3000 to 4000 ft/s, caps lower-velocity alluvium. Velocity inversions are a serious problem in seismic refraction work since they represent a blind zone. If unaccounted for, depth calculations for deeper refractors can be greatly overestimated. The accommodation of undetected layers with the arrival time data alone is discussed in the next chapter.

### Assigning Arrival Times to Refractors

Assigning arrival times to refractors can be done by inspection of the travel time curves. For the geological case of layers with planar interfaces and discrete seismic velocities increasing with depth, a travel time curve will consist of a series of straight-line segments where each subsequent segment represents arrival times from a deeper, faster layer. The segments of reciprocated travel time curves corresponding to the same layers will have nearly the same apparent velocity. Using travel time expressions derived for such cases (e.g., Mota, 1954), a depth section can be easily determined.

Deviation of the subsurface geology from plane interfaced layers will result in irregular travel time curves. In order to resolve the ambiguity in assigning arrival times to refractors, some data redundancy is required in addition to considerations for reciprocated shots.

The travel time curves for the data collected over the 3300 ft profile are displayed in Figure 5. Assignment of the arrival times to different refractors is represented by the use of different symbols for the arrival time data points. The interpretation of data points as critical arrivals from the suballuvial bedrock pediment surface (Figure 5) is based on the relatively high apparent velocities observed

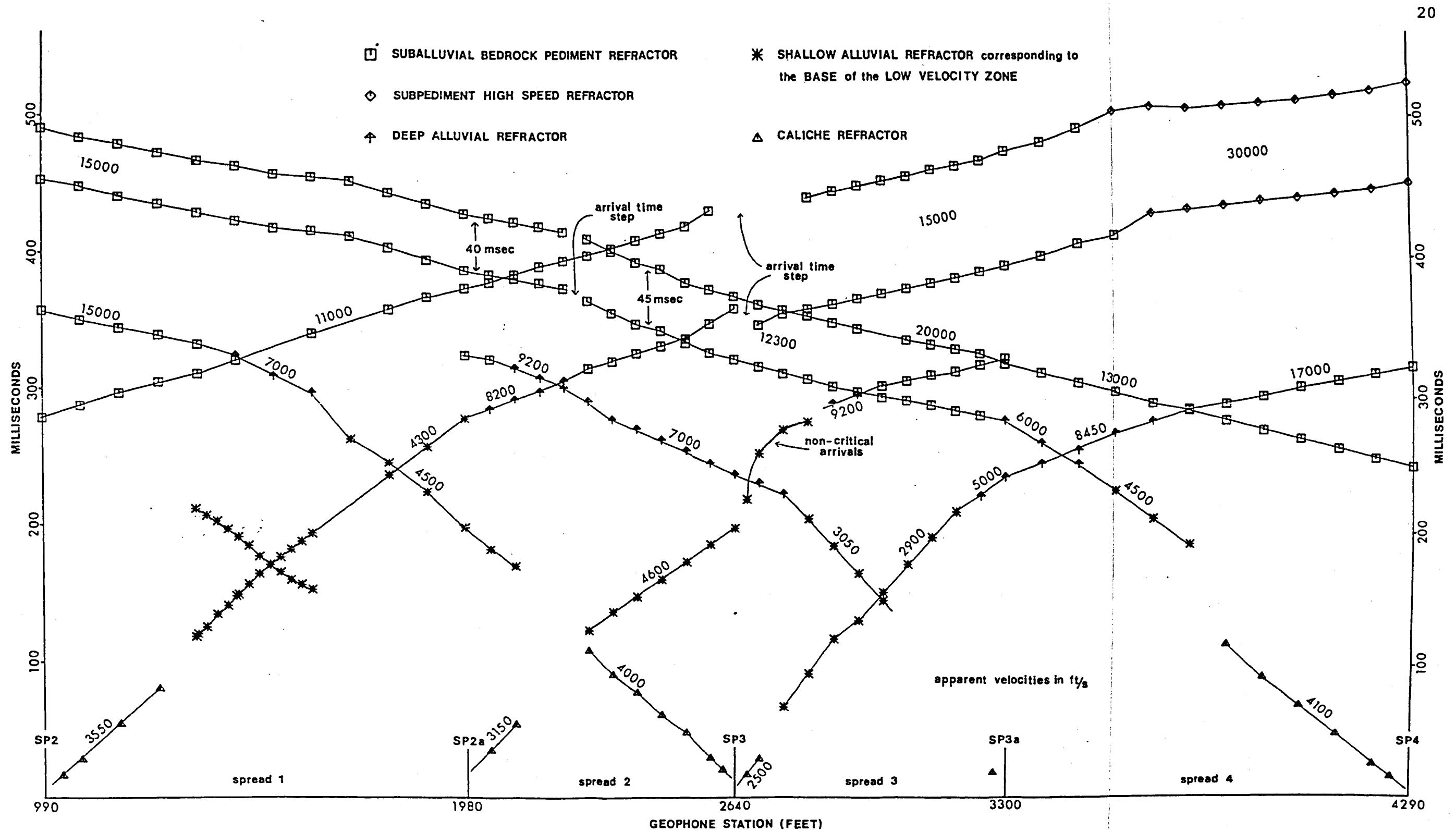


Figure 5. Dip line travel time curves.

and the extensive occurrence of these arrivals on the travel time curves.

The travel time data of the off-end shotpoints, 1 and 5 (the two reciprocated travel time curves of greatest delay shown in Figure 5), are the additional data needed in resolving the ambiguity of increasing apparent velocity with increasing distance from the shotpoints. Such changes in slope may correspond to either a change in dip and/or velocity and/or overburden velocity of the same refractor, or arrivals from a deeper, faster refractor. Comparison of the travel time curves of the off-end shots 1 and 5 with the end shots of the same direction, 2 and 4 respectively, permits the distinction. If a change in slope on the end shots represents a crossover distance, the corresponding change in slope on the more distant off-end shots will occur displaced towards that shotpoint. Changes in slope due to lateral refractor variations, on the other hand, will occur at the same geophone stations for both shots (Hawkins, 1961). Distinction of the lateral refractor variations of dip, velocity or overburden velocity is accomplished in the interpretational method that follows (Chapter 4).

The parallelism of the various travel time curves shown in Figure 5 indicates, then, that these arrival times correspond to critically refracted energy from the same surface. A very high-speed refractor with an apparent

velocity of 30,000 ft/s is sampled on the upthrown side of the fault scarp (Figure 5) from shotpoints 1 and 2. These arrivals are from a refractor below the pediment surface, as indicated by the changes in slope from shotpoint 1 occurring 90 ft before that of shotpoint 2 (Figure 6). Also, the travel time curve of shot 3 over this same area (spread 4) has an apparent velocity comparable to the pediment surface sampled elsewhere (Figure 5).

The high-speed refractor is never sampled shooting basinward from shotpoints 4 and 5, but some of the critical arrivals from the suballuvial pediment have taken a partial travel path along it. This is necessary by the equality of reciprocal travel time of shotpoints 2 and 4.

The difference in time between the parallel travel time curves of shots 4 and 5 changes from 45 msec to 40 msec at geophone station 2220 (Figure 5). This indicates that critical arrivals from the bedrock refractor at all the geophone stations from 2220 to 990 have taken a partial travel path along the deeper high-velocity refractor shooting basinward. Sampling of the suballuvial pediment surface across the entire 3300 ft profile for both directions of shooting has been accomplished in sum by various shots, but the whole profile reciprocal time along the pediment surface is not shown. This time-term, essential in determining the

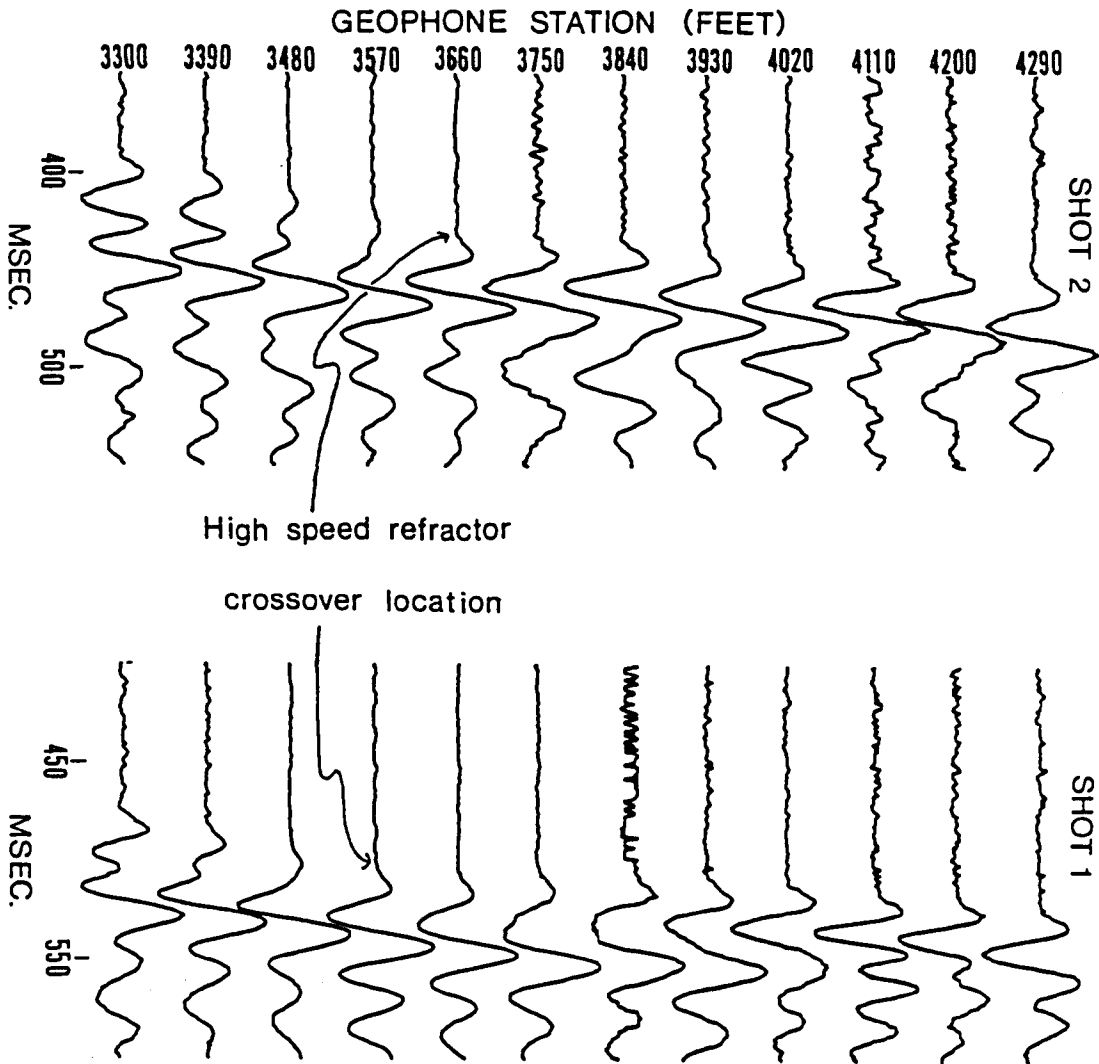


Figure 6. Shot records of shotpoints 1 and 2 over spread 4.

depth profile of the refractor surface, was solved for in a heuristic approach.

Shooting basinward, there is a step in the arrival times from the bedrock refractor at geophone stations 2280 to 2220. Shooting rangeward, there is also a step in the bedrock arrival times, but in the opposite sense, at geophone stations 2640 to 2700 (Figure 5). These reciprocal arrival time anomalies, corresponding to a step in the refractor (at least in the time domain), should be equal in magnitude. The anomaly shooting basinward is 4 msec less from shotpoint 4 than from the rangeward shot shotpoint 2. The arrival times at geophone stations 990 to 2220 from shotpoint 4, then can be shifted up 4 msec to correct for the partial travel time along the high-speed refractor.

With the whole profile reciprocal travel time for the bedrock refractor known, a set of composite reciprocal arrival time curves corresponding to common reverse coverage of the suballuvial pediment surface across the entire profile can be constructed from a combination of the curves shown in Figure 5. Starting with the bedrock arrival times of the end shots 2 and 4, arrival times before the crossover distances can be phantomized by shifting the corresponding arrival times of the respective off-end shots 1 and 5 down by the time difference between the common coverage geophone stations. Arrival times over spread 4 of shot 2 from the high-speed

refractor (Figure 5) were replaced by phantoming the bed-rock arrival times of shot 3, spread 4 to the corrected reciprocal time of shots 2 and 4.

From this composite reciprocal arrival time data alone, the refractor surface can be determined in depth using a seismic refraction interpretation technique called the generalized reciprocal method.

## CHAPTER 4

### THE GENERALIZED RECIPROCAL METHOD OF SEISMIC REFRACTION INTERPRETATION

The generalized reciprocal method (GRM) is a technique for mapping irregular refractors from in-line seismic refraction data (Palmer, 1980). It follows an interpretational phase where arrival times are assigned to refractors. A refractor can be mapped using the GRM under the extent of a set of surface receivers where arrival times from reciprocal shots are both from that refractor, and the shot-to-shot travel time along that refractor is known. A time-depth, calculated at each geophone location, is converted to a perpendicular distance from the refractor to the receiver station. These depth values are plotted as loci with respect to the receiver station. The envelope of arcs is taken as the best-determined refractor surface. Accurate depths to a refractor can be obtained for horizons dipping up to about 20 degrees.

A comprehensive discussion of the GRM is presented by Palmer (1980). Here the general concepts of the method will be introduced along with its application to the composite arrival time data of the bedrock refractor. The conventional reciprocal method (Hagedoorn, 1959; Hawkins,

1961), which is just a special case of the GRM, is discussed first to introduce the concepts of time-depths and velocity analysis of a refractor.

### The Conventional Time-depth

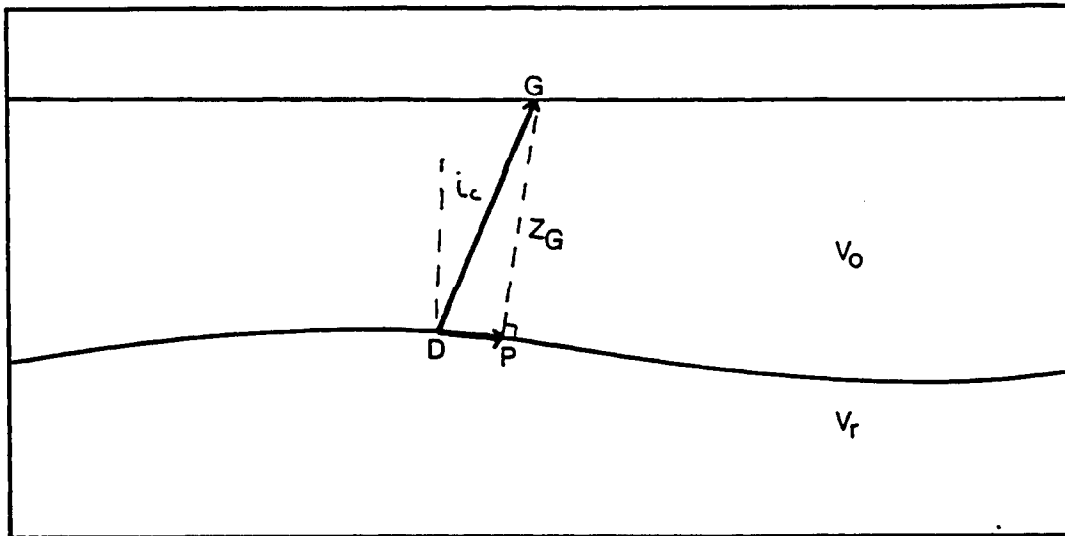
The conventional time-depth to a refractor is the delay time (Barry, 1967) associated with the emergent critical ray from the refractor to the surface receiver. More precisely, the time-depth to a refractor is defined as the travel time of the emergent critical ray path between the refractor and surface, minus the time associated with the length of the upward critical ray path projected onto the plane of the refractor to travel at the refractor velocity (Hawkins, 1961).

In Figure 7a, the time-depth  $t_g$ , at geophone station G is

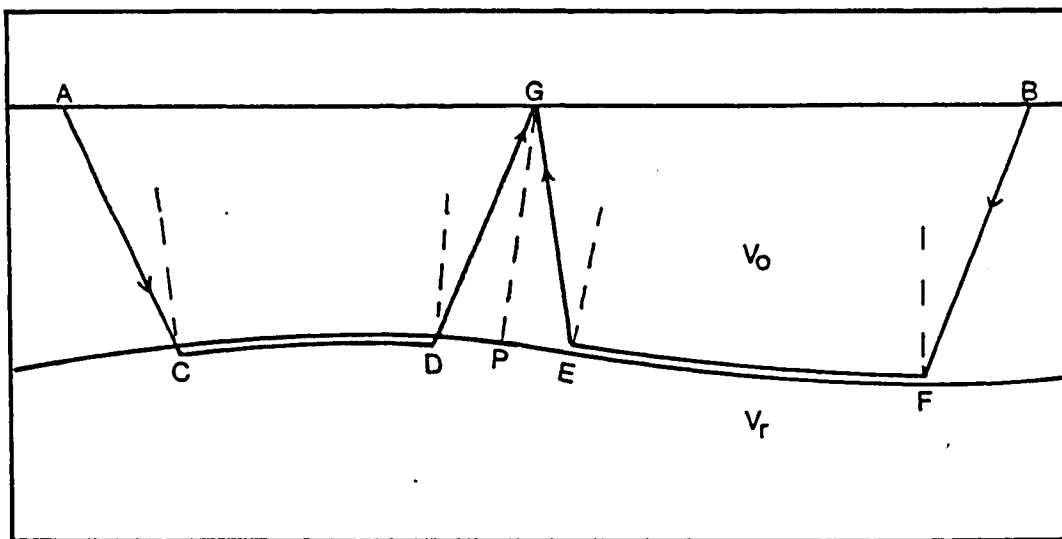
$$t_g = (DG/V_o - DP/V_r) \quad (4-1)$$

where  $V_o$  is the surface layer seismic P-wave velocity and  $V_r$  is the refractor seismic P-wave velocity.

Although the time-depth is by definition similar to the receiver delay time (Barry, 1967), the method of separating it from the arrival times and the appropriate field data to do so is different. When a spread of geophones is shot both forward and reversed, the time-depth to the refractor which corresponds with the shot-to-shot reciprocal



(a)



(b)

Figure 7. Ray paths of conventional time-depth. --  
 (a) Definition; and (b) Calculation.

time can be calculated at each geophone location which receives reciprocated critical rays from that refractor. At each appropriate geophone station, the time-depth is obtained by adding the arrival times from each shotpoint, subtracting the reciprocal time, and halving the results.

From Figure 7b, the time-depth  $t_g$ , at the geophone station G is

$$t_g = 1/2(t_{AG} + t_{BG} - t_{AB}) \quad (4-2)$$

where  $t_{AG}$  and  $t_{BG}$  are the arrival times of the critical rays at G from shots A and B respectively, and  $t_{AB}$  is the reciprocal time for the refractor.

The above travel time expression can be written in terms of the segment travel times as distance/velocity. From Figure 7b, then, equation (4-2) reduces to

$$t_g = 1/2(DG/V_o + EG/V_o - DE/V_r) . \quad (4-3)$$

If the refractor is assumed to be a plane between the two points of emergence, D and E, then from symmetry, equation (4-3) reduces to

$$t_g = (DG/V_o - DP/V_r)$$

which is the time-depth expression of equation (4-1).

From the geometry of Figure 8, it is seen that the time-depth can be expressed in terms of depth and critical angle of incidence as



$$t_g = Z_G \cos i_c / V_o$$

where  $Z_G$  is the perpendicular distance from the plane of the refractor to the geophone G, and  $i_c$  is the critical angle of incidence as defined by Snell's Law. The above equation can be rearranged to

$$Z_G = t_g V_o / \cos i_c$$

where the term  $V/\cos i_c$  is the depth conversion factor for the two-layer case illustrated in Figures 7 and 8. For the more common case of a refractor overlain by more than one layer, a depth conversion factor which accounts for all the overlying layers' thicknesses and velocities must be determined or a composite overburden velocity term calculated from other sources such as reflection data, velocity logs, drill hole depths, etc. (Hawkins, 1961).

The refractor velocity for an undulating horizon can be determined from the arrival times and time-depths alone. By subtracting the time-depth from the arrival times at a geophone station, the effect of variations both in refractor depth and overlying velocity is removed. This corrected arrival time is then the shotpoint delay time plus the travel time along the refractor to the point where the normal to the refractor passes through the geophone. Illustrated from Figure 7b, the corrected arrival time  $t'_{AG}$ , from shotpoint A to geophone station G is

$$t'_{AG} = t_{AG} - t_g \quad (4-4a)$$

where  $t_{AG}$  is the observed arrival time and  $t_g$  the time-depth. Expressed in terms of the segment travel times, this equation reduces to

$$t'_{AG} = (AC/V_o + CD/V_r + DG/V_o) - 1/2(DG/V_o + EG/V_o - DE/V_r), \quad (4-4b)$$

and from the symmetry assumed in the time-depth expression of equation (4-3)

$$t'_{AG} = (AC/V_o - CP/V_r). \quad (4-4c)$$

For adjacent geophones, the difference in these corrected times is the travel time along the refractor between their respective points where the normal to the refractor passes through them. The refractor velocity is taken to be the inverse slope of a line fitted to the corrected arrival times plotted against geophone location. The inverse slope will deviate from the true refractor velocity because the point on the refractor corresponding to the distance along the normal to the refractor to the respective geophone station is not known. The time-depth calculation determines a loci value and not an actual depth point below the geophone station. Determination of the refractor velocity can be improved after the refractor surface has been determined as the envelope of arcs of appropriate radii (depth values).

The corrected arrival times are then migrated to their location on the envelope, and the new time versus distance plot gives a better estimate of refractor velocity (Hawkins, 1961).

There is still some error inherent in the refractor velocity determination because of the assumption of symmetry between emergent critical rays in the calculation of the time-depth. Also, the loss of refractor detail between emergent critical rays renders the conventional reciprocal method inadequate for mapping irregular deep refractors as the distance between reciprocal emergent critical rays becomes greater. The generalized time-depth  $t_G$ , and the velocity analysis function  $t_V$ , of the GRM overcome this loss of detail problem by determining the reciprocal arrival times which corresponds with the critical rays emerging near the same point on the refractor.

#### The Generalized Time-depth and Velocity Analysis Functions

From Figure 9, the generalized time-depth function  $t_G$ , at G, is defined by Palmer (1980) by the equation

$$t_G = 1/2[t_{AY} + t_{BX} - (t_{AB} + XY/V_r')] \quad (4-5)$$

where  $V_r'$  is the best-determined refractor velocity,  $t_{AY}$  is the arrival time at Y from shotpoint A,  $t_{BX}$  is the arrival

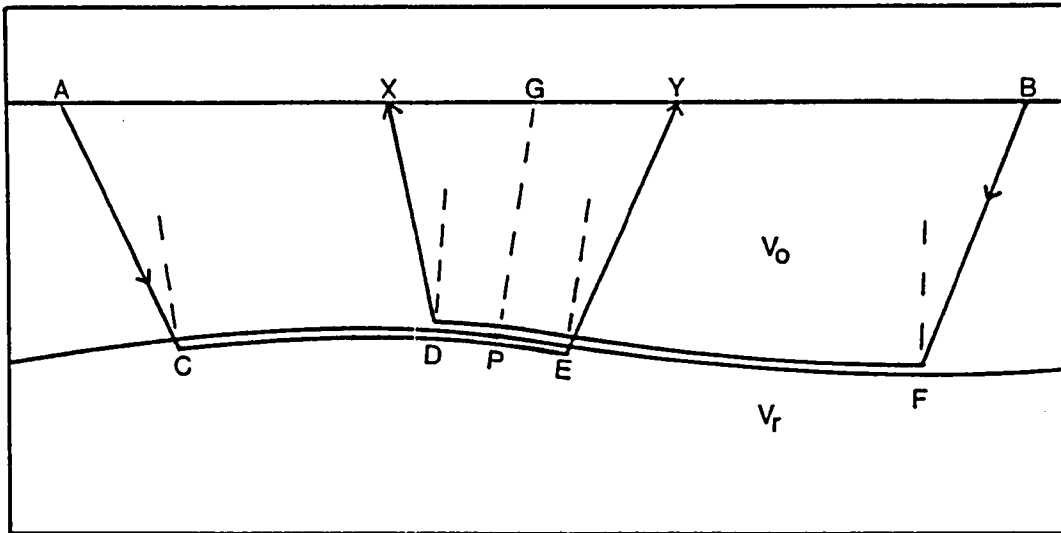


Figure 9. Ray paths in calculation of generalized time-depth.

time at X from shotpoint B, and  $t_{AB}$  is the reciprocal travel time of shotpoints A and B.

The generalized time-depth function is identical to the conventional time-depth function when XY equals zero. The extra term  $XY/V_r'$  of the generalized time-depth is to account for the extra travel time along the refractor.

Because of this extra term, the value  $V_r'$  must first be determined from the velocity analysis function  $t_V$ . Again, using the symbols of Figure 9, the velocity analysis function  $t_V$  is defined by the equation

$$t_V = 1/2(t_{AY} - t_{BX} + t_{AB}), \quad (4-6a)$$

and its value is referred to G, the midpoint of X and Y.

For the case of XY equal to zero, equation (4-6a) is equal to equation (4-4a). Equation (4-6a) expressed in terms of the segment travel times as distance/velocity reduces to

$$t_V = 1/2(AC/V_o + CD/V_r) + 1/2(DE/V_r + EY/V_o - DX/V_o). \quad (4-6b)$$

As in equation (4-4b), the segment travel time between emerging critical rays (in the general form, this segment,  $DE/V_r$ , varies with the XY-value and can be positive or negative) is assumed to occur along a planar surface, and the emergent travel times,  $DX/V_o$  and  $EY/V_o$ , are assumed equal, therefore from symmetry

$$t_V = (AC/V_O + CP/V_R) \quad (4-6c)$$

at G.

In determining the best refractor velocity  $V_R'$ ,  $t_V$  is calculated using equation (4-6a) and plotted against distance for a series of different XY-values. For a given velocity structure above a surface of refractor velocity  $V_R$ , some XY-value corresponds with the emerging critical rays leaving the refractor at near the same point. This XY-value is called the optimum XY. From Figure 9, it can be seen that at the optimum XY, points D and E coincide, and the assumption of the segment travel time  $DE/V_R$ , occurring along a planar surface is minimized. The best-determined refractor velocity  $V_R'$  is usually taken as the inverse slope of a line fitted to the  $t_V$  values for the optimum XY.

An improved estimate of  $V_R'$  can be obtained, as discussed above, after determining the refractor surface by migrating the  $t_V$  values to their correct position on the refractor. If the refractor is near planar, an improved  $V_R'$  can simply be obtained using equation (9) of Palmer (1980, p. 9).

Once  $V_R'$  is obtained, the generalized time-depth  $t_G$  (from now on referred to as time-depth) is calculated at each geophone station with the appropriate arrival times and plotted against distance. As with the velocity analysis

function  $t_V$ , the time-depth function is plotted for a series of XY-values. Two computer programs were written, TVEL and TDEPTH, in Fortran 77 to facilitate the calculating and plotting of  $t_V$  and  $t_G$  respectively. Figures 10 and 11 are examples of the output of the programs for the arrival times of the bedrock refractor. For both plots, each set of points corresponds with the respective functions being calculated at each geophone station for some XY-value. The bottom set of points for the velocity analysis functions of Figure 10 correspond with  $t_V$  calculated at XY equal to zero. For each subsequent set of points the XY-value is incremented by some given value (in this case 60 ft). The time-depth plot of Figure 11 is analogous except here the time axis is inverted and XY equal to zero corresponds with the top set of points. Each time the XY-value is incremented, the total reciprocal time  $t_{AB}$ , is incremented to prevent overlap of adjacent curves. This results in a vertical displacement of points.

By examination of the velocity analysis and time-depth functions for a series of trial XY-values, an optimum XY can be determined if the refractor is sufficiently irregular. For the optimum XY, the velocity analysis curve should be simplest and the time-depths most detailed. Selection of optimum XY-values is discussed below with application to the bedrock refractor. For a featureless or near-featureless refractor, the assumption of a planar surface

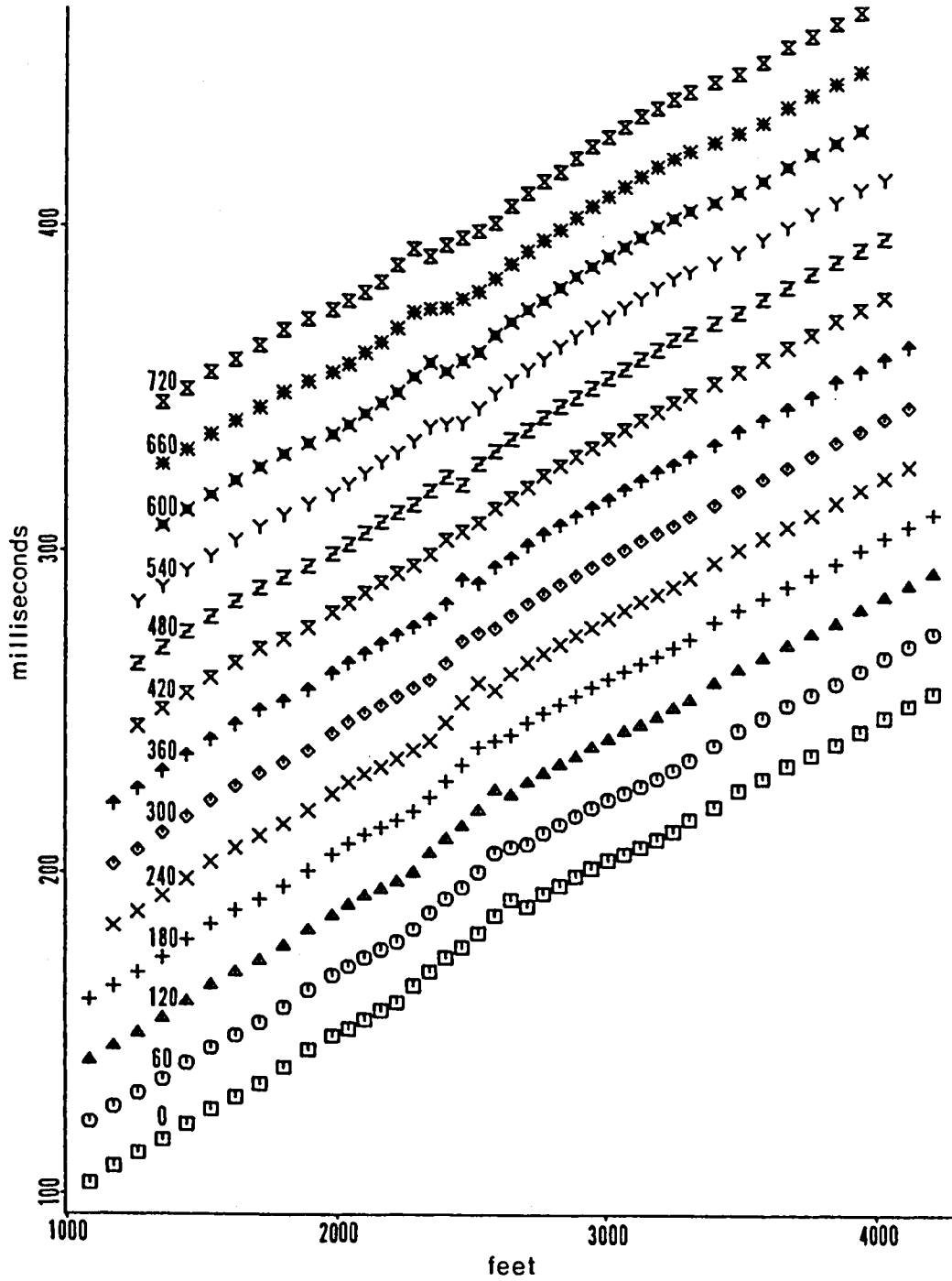


Figure 10. Velocity analysis curves derived from arrival times of the bedrock refractor.

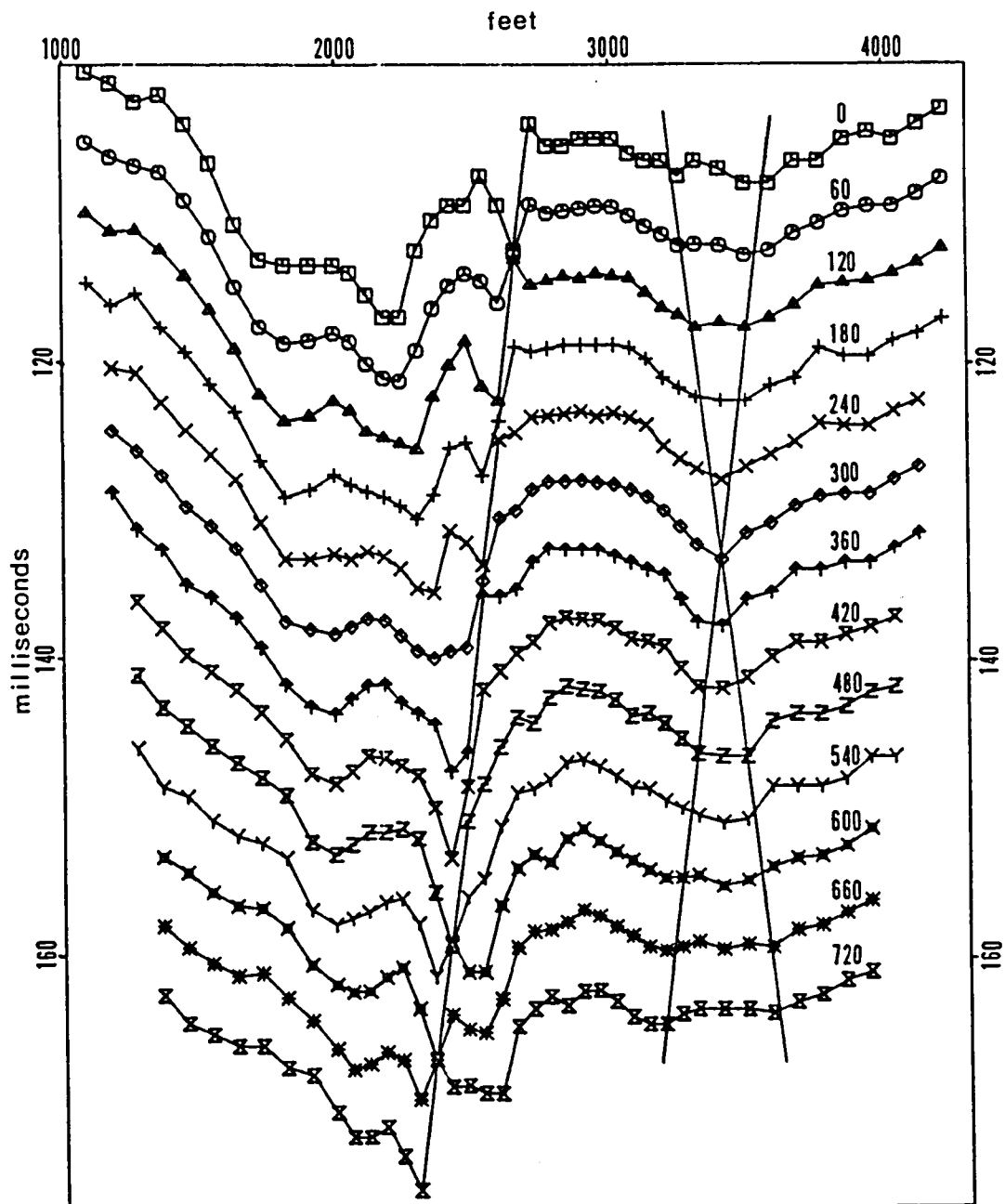


Figure 11. Time-depths derived from arrival times of the bedrock refractor.

between emergent critical rays is a good one, and so the determination of an optimum XY-value will not be possible nor necessary for mapping the refractor (provided the depth conversion factor is known). However, full presentation of GRM parameters also permits the recognition of lateral variations in thickness and/or velocity of near-surface layers, and the separation of these inhomogeneities from deeper irregularities (Palmer, 1980).

An arrival time anomaly caused by a near-surface inhomogeneity, which extends at most over only a few geophone intervals, will occur at near the same geophone location for reciprocal shots, since in the shallow part of the section the upgoing critical rays from opposite directions pass through near the same material. Forward and reverse raypaths traveling through deeper inhomogeneities, such as a refractor irregularity, are further separated on the arrival time curves. Because of the assumed symmetry in travel time of the upward critical raypaths in calculation of the time-depths, time-depth anomalies are only equal to arrival time anomalies when the XY-separation is equal to the arrival time separation. For other XY-values the time-depth anomaly is one-half the arrival time anomaly and smoothed out over a distance of  $1/2 \Delta XY$  on both sides of the source of the anomaly.

An example of this effect can be seen in the time-depth plot of Figure 11 at geophone station 3390. At XY equal to 300 ft the depression in the curve is sharpest. For the XY-values 120 ft and 480 ft (i.e.,  $\Delta XY$  equals 180 ft), the anomaly is halved and flattened out 90 ft on each side of station 3390.

Palmer (1980, p. 32) demonstrates, using a variety of synthetic models, the recognition of nearly inseparable surface and refractor anomalies of the travel time curves with time-depth and velocity analysis plots similar to Figures 10 and 11.

Evidence for a shallow anomaly with respect to the bedrock refractor will be demonstrated below.

#### Determining the Average Velocity Above a Refractor

One of the most powerful features of the GRM is the determination of an average overburden velocity for a refractor from an optimum XY-value, the time-depths, and refractor velocity. This allows the conversion of time-depths to depth values without delineating all the thicknesses and velocities of layers above a refractor. Depth conversion using an average velocity determined from GRM parameters is generally more accurate than using a velocity structure obtained from elementary interpretation of travel time curves (Palmer, 1980, pp. 46-47).

With the recognition of a velocity inversion, inferred from the arrival time discontinuities on the field records, and the lack of other data such as drill hole depths, velocity logs or uphole shots from the base of the LVL, the determination of an average overburden velocity is the only reasonable means of depth conversion for the time-depths of the bedrock refractor.

Even with no velocity inversion above a refractor, it is essentially impossible to determine an accurate overburden velocity from refraction data alone (Hagedoorn, 1959). The possible presence of hidden layers, undetected because energy from deeper layers arrives at the surface first, will result in depth values calculated from first arrival data being too shallow. For any given first-break arrival time curves, there is a blind zone between any two recognized layers in which a hidden layer can exist of thickness varying from zero to some theoretical maximum (Hawkins and Maggs, 1961). It has also been numerically demonstrated by Hagedoorn (1955) that linear, parabolic, exponential and discrete layer velocity distributions can satisfy the same first-arrival data within the usual error of refraction work. Because refraction first-arrival data only samples an upper portion of each recognized layer, there is a blind zone for every layer, whether a hidden layer exists or not, represented by the unsampled portion where the velocity distribution is extrapolated.

Palmer (1980, Chapter 8) derives an average velocity expression from GRM parameters for a planar horizontal n-layer case. The accuracy of such determined overburden velocities are considered good for dips up to 20 degrees.

Using the symbols of Figure 12, the average overburden velocity  $\bar{V}$ , and an angle  $\bar{i}_c$  are defined such that

$$\sin \bar{i}_c = \bar{V}/v_r', \quad (4-7)$$

$$t_G = (\cos \bar{i}_c / \bar{V}) \sum_{j=1}^{n-1} z_{jG}, \quad (4-8)$$

and since at the optimum XY separation, forward and reverse emergent rays leave the refractor at near the same point,

$$XY = 2 \cdot \tan \bar{i}_c \sum_{j=1}^{n-1} z_{jG} \quad (4-9)$$

where  $\sum_{j=1}^{n-1} z_{jG}$  is the sum of layer thicknesses above the refractor at station G.

Equations (4-8) and (4-9) arranged in terms of the depth to the refractor  $\sum z_{jG}$ , forms the relationship

$$\bar{V} t_G / \cos \bar{i}_c = XY / 2 \tan \bar{i}_c$$

where XY is the optimum XY. The average velocity

$$\bar{V} = XY \cdot \cos \bar{i}_c / 2 \cdot t_G \tan \bar{i}_c,$$

reduces to

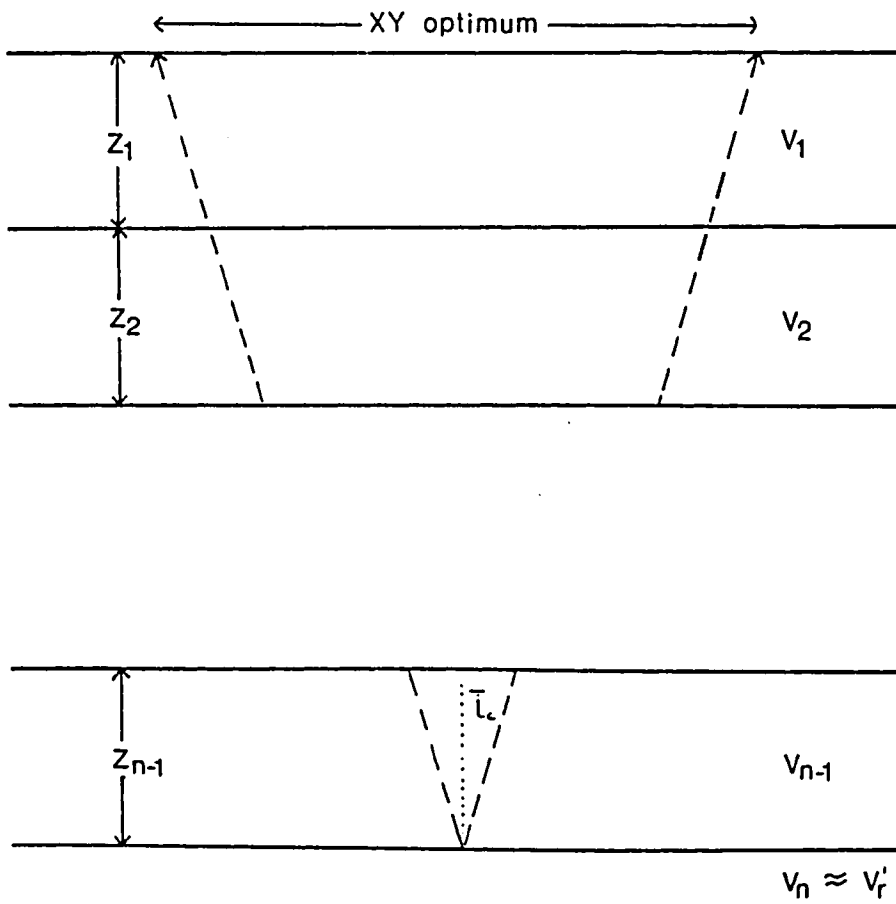


Figure 12. Symbols used in definition of the average velocity above  $n$ th horizon.

$$\bar{v} = \sqrt{v_r'^2 \cdot XY / (XY + 2t_G v_r')} \quad (4-10)$$

when the trigonometric functions are expressed in terms of velocity.

The time-depth  $t_G$ , in equation (4-10) should be the average time-depth to the refractor over some segment of the refraction profile where an optimum XY-value is well determined.

The depth conversion factor,

$$\bar{v} v_r' / \sqrt{v_r'^2 - \bar{v}^2}, \quad (4-11)$$

from equation (4-8), when substituted with equation (4-10), reduces to

$$\sqrt{v_r' \cdot XY / 2 \cdot \bar{t}_G} \quad (4-12)$$

where  $\bar{t}_G$  is the average time-depth value of equation (4-10).

Accurate determination of the average velocity is most dependent on the accuracy of the XY-value. The accuracy of the XY-value is dependent on the refractor being sufficiently irregular and the spatial resolution of the geophones. Determination of an optimum XY is not necessary for accurate depth calculations provided that overburden velocities are known. Determination of overburden velocities from refraction data alone, however, is subject to large uncertainties. The average velocity term, like the empiri-

cally determined RMS velocity from trial and error normal-move-out corrections made on reflection data, is dependent on determining travel paths which have sampled all of the overburden. If no other velocity information is available, determination of the optimum XY-value becomes essential for the derivation of a depth conversion factor which will not be adversely affected by the possible presence of hidden layers or velocity inversions (Palmer, 1980).

#### Determination of the Bedrock Surface using the GRM

In the preliminary interpretation of the previous chapter a composite arrival time curve corresponding to common reverse coverage of the suballuvial bedrock surface across the entire 3300 foot profile was constructed. The only correction made to this and the other travel time data was a shot hole correction. A datum plane correction is not necessary since individual depth values are determined with respect to each geophone station. The arrival times input to programs TVEL and TDEPTH are the bedrock arrival times corrected for the uphole travel time. If an arrival time for a geophone station was missing for one direction of shooting such as station 1710 of shot 1, a zero was entered into the data set. The programs TVEL and TDEPTH search for the next non-zero station and linearly interpolate a value for the missing channel.

### Determining Optimum XY-values

As stated above, optimum XY-values can be determined from inspection of the velocity analysis and time-depth curves. The velocity analysis curves for the bedrock refractor at XY-values ranging from zero to 720 ft are illustrated in Figure 10. At or near station 2460 the velocity analysis function curve straightens out for XY equal to 420 ft. The velocity analysis function curves for other XY-values depart from a straight line over a short interval. This characteristic pattern is caused by the step or fault in the bedrock corresponding with the steps in the arrival time at stations 2640 and 2220 of Figure 5, and is an excellent indicator of the optimum XY-value. At the optimum XY-value, the velocity analysis curve is a straight line. At other than optimum XY-values the curves deviate from a straight line because of the lack of symmetry in travel times of reciprocal emergent raypaths on each side of the fault. The optimum value of 420 ft can be determined, in this case, from the travel time curves themselves. This results because the steps in the arrival times, separated by 420 ft, are so obvious.

Figure 13 shows the velocity analysis curves at XY-values ranging from zero to 420 ft. The time scale is expanded to show greater detail. Three refractor velocity values  $V_r^1$  were determined: 12,700 ft/s from stations 990 to 2220; , 11,200 ft/s between stations 2220 and 2820; and

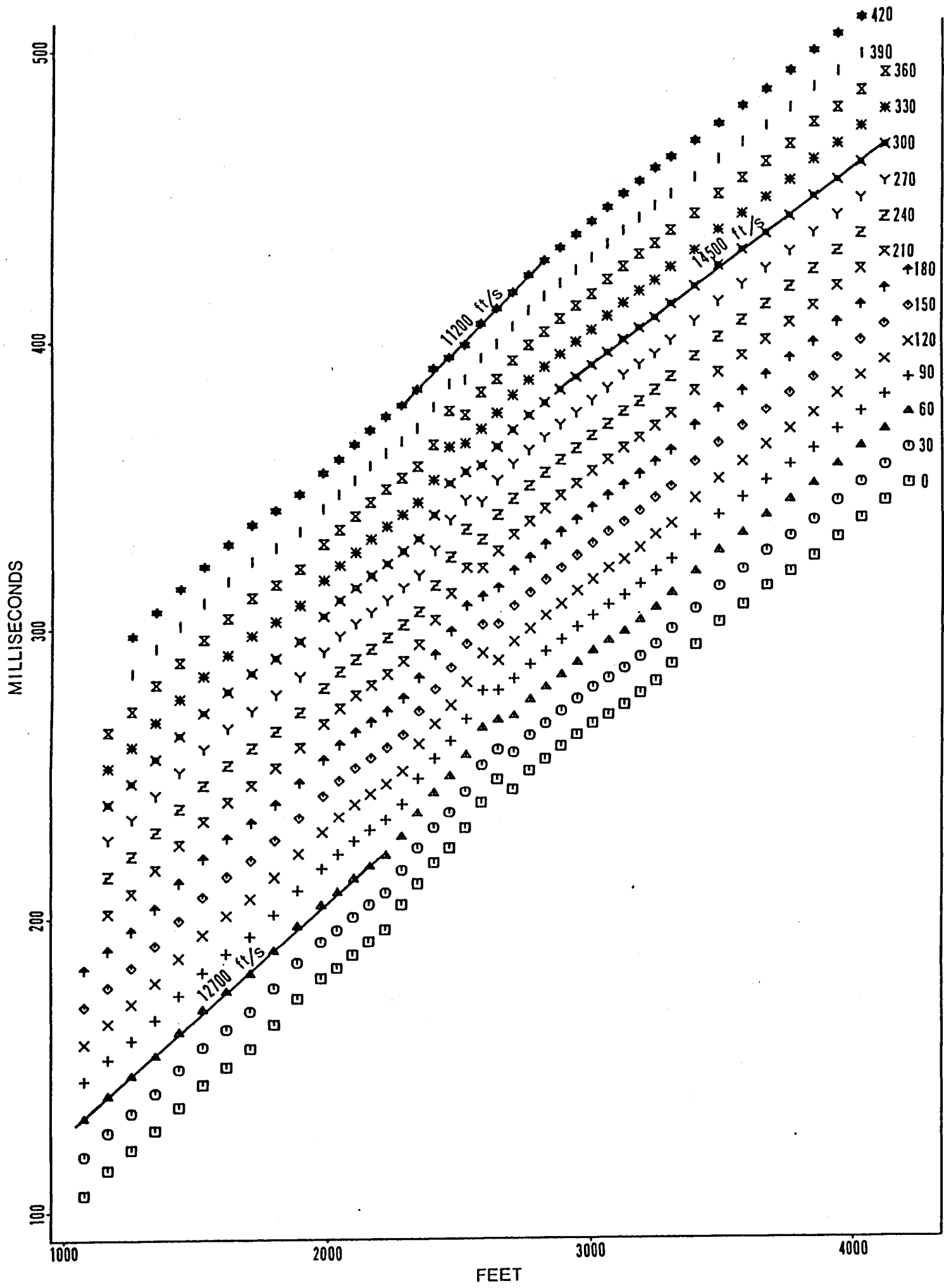


Figure 13. Bedrock velocity analysis curves at expanded time scale.

14,500 ft/s from stations 2280 to 4290. These three refractor velocities correspond with the downthrown side of the fault, the fault zone, and the upthrown side of the fault, respectively, and are listed in Table 1. The velocity values given are the inverse slopes of the least squares fit to the designated data points, rounded to the nearest 100 ft/s. The lateral change of refractor velocity on each end of the fault zone was smoothed over six geophone intervals by linearly interpolating the refractor velocity determined on each side. This was done because there would be a transition zone where the velocity in the term  $XY/V_r'$  of the time-depth equation (equation 4-5) would be of some intermediate value. The transition zone of six geophone intervals was used because it was found that a line segment of intermediate slope could be fitted over approximately that many stations.

Although the curve is most linear over the fault zone for  $XY$  equal to 420 ft, it is not on each end of the profile. Optimum  $XY$ -values will vary over the length of a profile if the refractor velocity and/or the overburden velocity varies laterally. The optimum  $XY$ -value of 420 ft, then, only pertains to the fault zone since the refractor velocity changes away from the fault. It is desirable to determine optimum  $XY$ -values on each side of the fault not only to delineate maximum refractor detail but more importantly to independently determine an average overburden velocity for each side.

Table 1. Bedrock refractor velocities  $V_r'$ , and optimum XY-values.

Location (Geophone Stations)	$V_r'$ (ft/s)	XY Optimum (ft)
999-2220	12,700	~390
2280-2820	11,200	420
2880-4290	14,500	300

Differential sedimentation due to growth faulting may result in different velocity structures on each side of the fault, and hence different depth conversion factors for the respective time-depths.

On the left-hand side of Figure 13, the curve appears most simple at XY equal to 60 ft. Such a low XY-value, compared to the optimum XY of 420 ft for the fault zone, suggests near-surface irregularities on the downthrown side of the fault. On the upthrown side of the fault, the velocity analysis curves look very similar over a range of XY-values. The value of 14,500 ft/s is shown at XY equal to 300 ft, but could be determined to within one percent of this value over several adjacent curves of Figure 13. The selection of 300 ft is based on analysis of the time-depth curves.

Determination of optimum XY-values over the more subtle refractor features away from the fault can be done by inspection of the time-depth curves. The range of time-depth values across the profile is much smaller than the range of velocity analysis function values. In consideration of plotting space, the time-depth curves permit use of a much greater time scale. It is therefore visually easier to confidently choose optimum XY-values based on refractor detail delineated on the time-depth curves than from the simplification of the velocity analysis curves.

The time-depths plotted at XY intervals of 30 ft, ranging from zero to 420 ft is illustrated in Figure 14. The most obvious feature of this plot is the large time-depth anomaly in the middle corresponding to the subsurface fault. To show the maximum detail in time-depths on each side of the fault, a time scale which results in overplotting of this feature was used.

Determining an optimum XY-value from time-depth curves should be based on delineation of refractor features which extend over several geophone intervals. An example of this is illustrated in Figure 14. On the upthrown side of the fault there is a depression in the refractor. This time-depth anomaly, as pointed out previously on Figure 11, is sharpest and maximized at XY equal to 300 ft. This is taken as the optimum XY for the refractor on the upthrown block of the fault. The depression, which is maximized at geophone station 3390, extends approximately from station 3000 to the rangeward end of the profile and is generally defined at all XY-values shown. Figures 14 and 11 clearly illustrate the progressive subdual of the refractor depression at the non-optimum XY-values, incrementing both less than and greater than XY equal to 300 ft. Refractor features of short wavelength with respect to a few geophone intervals will in most geologic cases be of a magnitude comparable to the uncertainty of the first arrivals. Short wavelength irregulari-

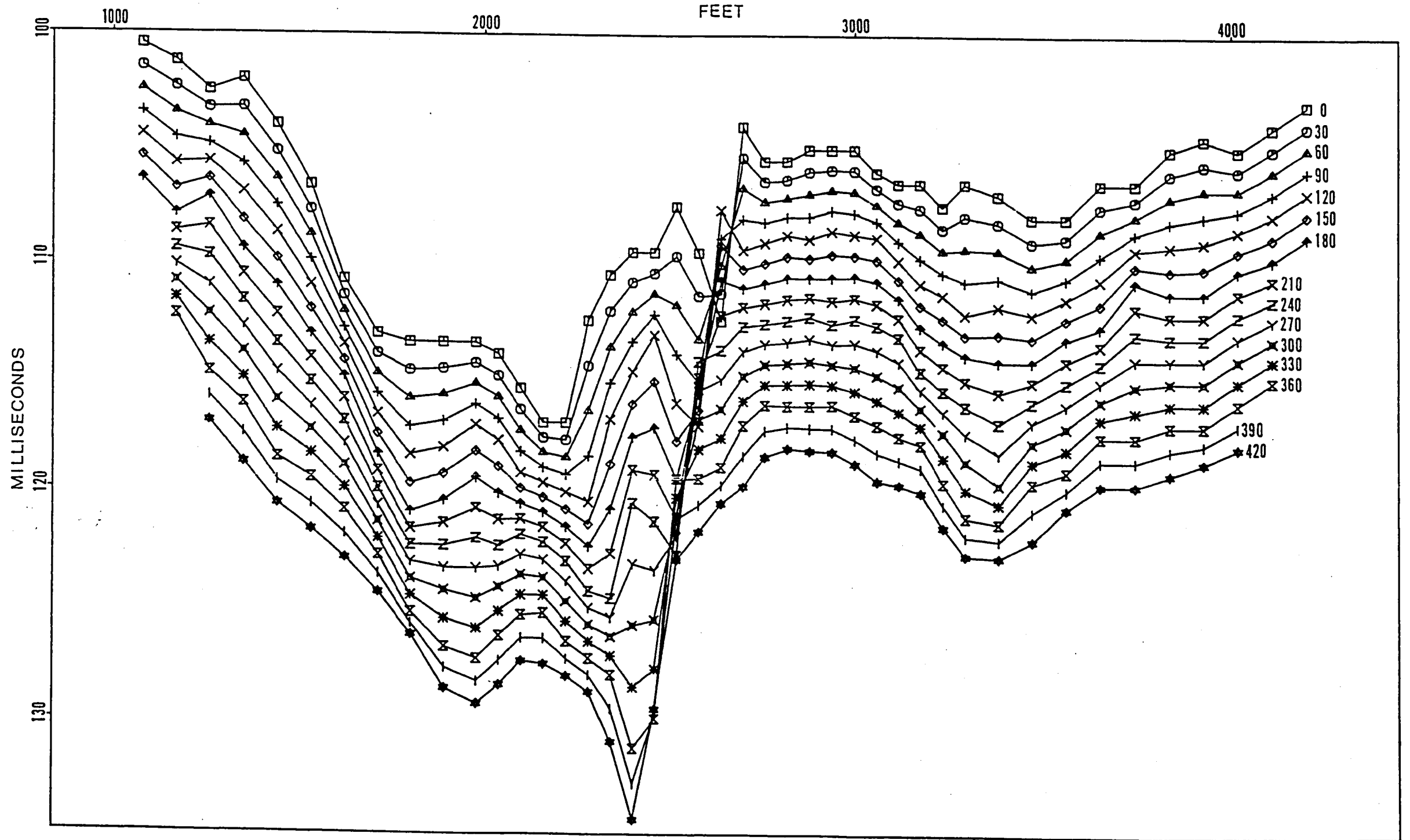


Figure 14. Bedrock time-depths at expanded time scale.

ties on the time-depth curves can result from a number of causes. If caused by near-surface inhomogeneities, the irregularity will be optimized at relatively small XY-values for reasons discussed above. Irregularities observed over only a few station intervals may also be due to unrelated near-surface anomalies being matched at higher XY-values or due to unrelated refractor anomalies being matched or any combination of unrelated arrival time irregularities. Long wavelength features with respect to geophone spacing are represented by systematic trends in the arrival time data. The respective long wavelength features represented on the time-depth curves will not be adversely affected by small errors in picking individual arrival times. It follows that determining optimum XY-values from more subtle refractor features will require a closer geophone spacing, but this in turn will be limited by the uncertainty of arrival times.

#### Removal of Near-surface Anomaly

Choosing an optimum XY on the basin side of the fault is complicated by the presence of near-surface or mid-depth anomalies. From geophone stations 1710 to 2160 there is a trough-crest feature in the time-depths which is optimized at XY equal to about 150 to 180 ft. For XY-values less than and greater than this, the trough-crest feature is reduced and smoothed. At XY-values greater than 270 ft, a similar

shaped anomaly occurs shifted towards the fault. This trough-shaped feature appears optimized over the XY-values 360 to 420 ft.

There are two anomalies, a shallow one and one along the refractor. Both anomalies are very subtle but are enhanced due to emergent raypaths from shotpoint 4 having sampled both regions. These anomalous arrival times correspond to the change in slope or arrival time delays occurring over geophone stations 1620 to 1800 from shotpoint 4 (Figure 15). Arrivals from the rangeward shot, shotpoint 2, show no comparable anomaly match (Figure 15). Emergent critical travel paths from shotpoint 2 sampling the shallow anomaly occur at closer offset receiver stations than the emergent rays sampling the refractor anomaly (Figure 15). The exaggerated anomaly of shot 4 is matched twice, resulting in optimization at an XY of about 180 ft and about 390 ft and migration of the time-depth anomaly with increasing XY (Figure 14). The sum of the shallow and refractor arrival time delays of shot 2 corresponding to the arrival time delays of shot 4, as suggested by the optimization of the time-depth curves (Figure 15), agrees to within one millisecond of the delays of shot 4. By subtracting the arrival time delays of shot 2 caused by the near-surface anomaly from the corresponding reciprocal stations 180 ft apart, the near-surface effect can be removed. The time-depth curves of

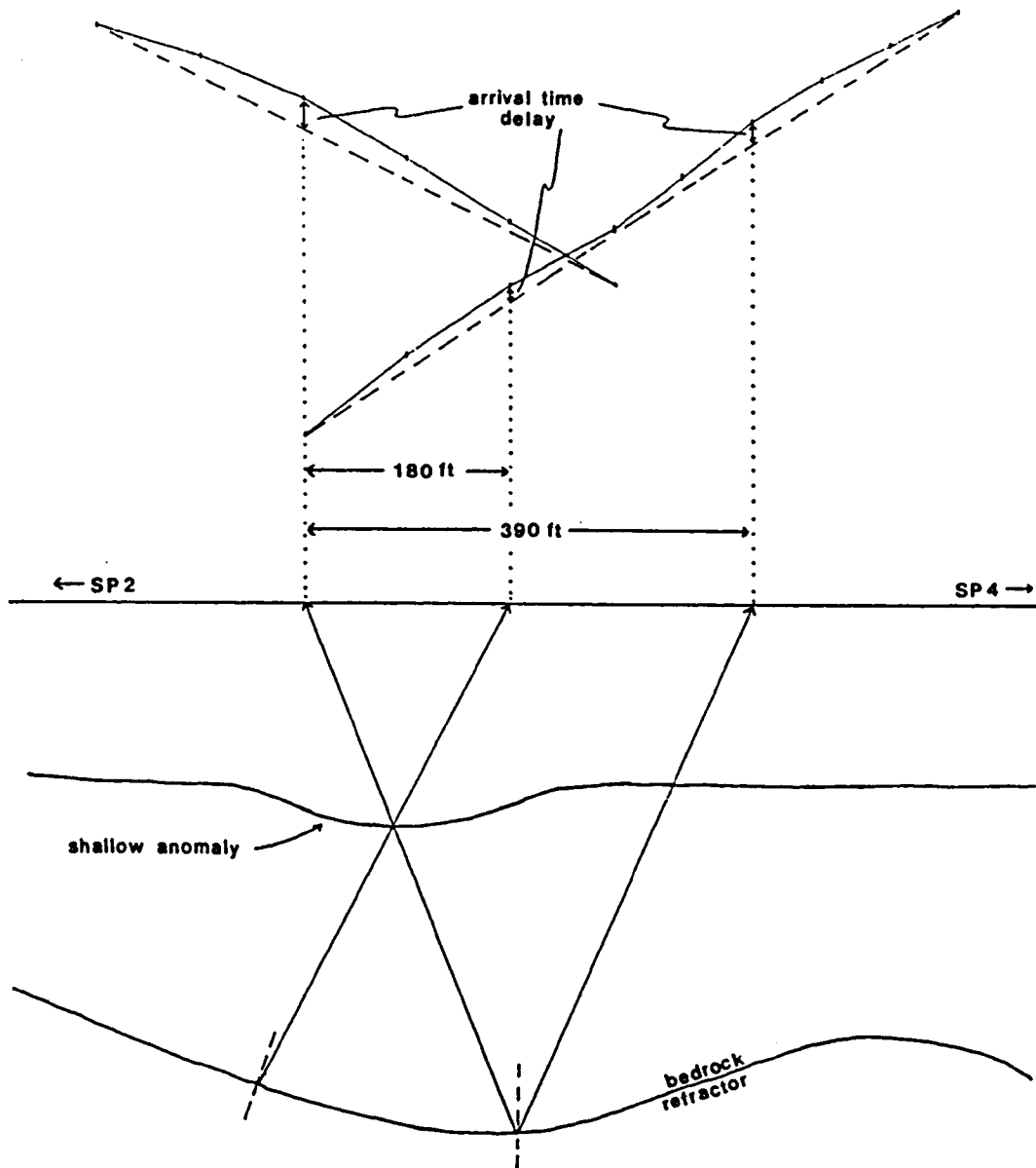


Figure 15. Schematic diagram of optimized ray paths with travel time data of the composite arrival time curves.

of Figure 16 for the corrected arrival times clearly illustrates the removal of the near-surface anomaly. The refractor trough-crest feature has been subdued, as expected, and is still optimized at about 360 to 420 ft. The subtlety of the feature does not permit a clear determination of an optimum XY. The median value of 390 ft seems reasonable considering that 420 ft was determined over the immediately adjacent fault zone and will further prove consistent with the other two values determined in consideration of overburden velocity. Further basinward of the trough-crest feature, the time-depth curves show little indication of near-surface inhomogeneities or deeper irregularities. The near-planar conditions of the refractor in this vicinity makes it impossible to determine an optimum XY-value.

Table 1 summarizes the XY-values.

The near-surface anomaly also results in the velocity analysis curves aligning best on the basin side of the fault for small XY-values because of the symmetry in time of reciprocal emergent rays at shallow depths (i.e., if both upgoing critical rays pass through the source of the anomaly, the effect is cancelled). The velocity analysis curves of Figure 17 for the corrected arrival times illustrates the simplification of the velocity analysis curves on the basin side of the fault for higher XY-values (compare with Figure

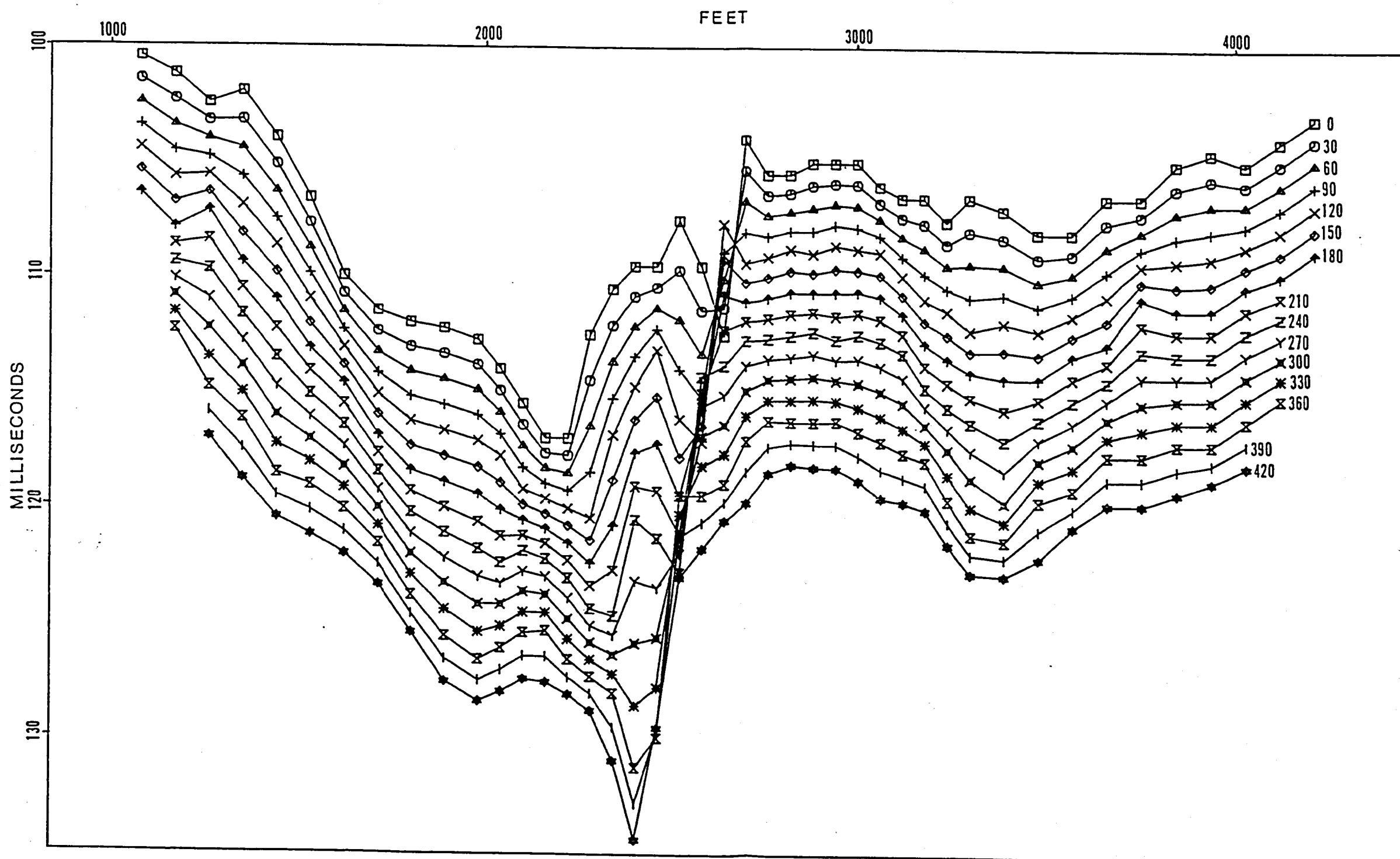


Figure 16. Bedrock time-depths after removal of shallow anomaly.

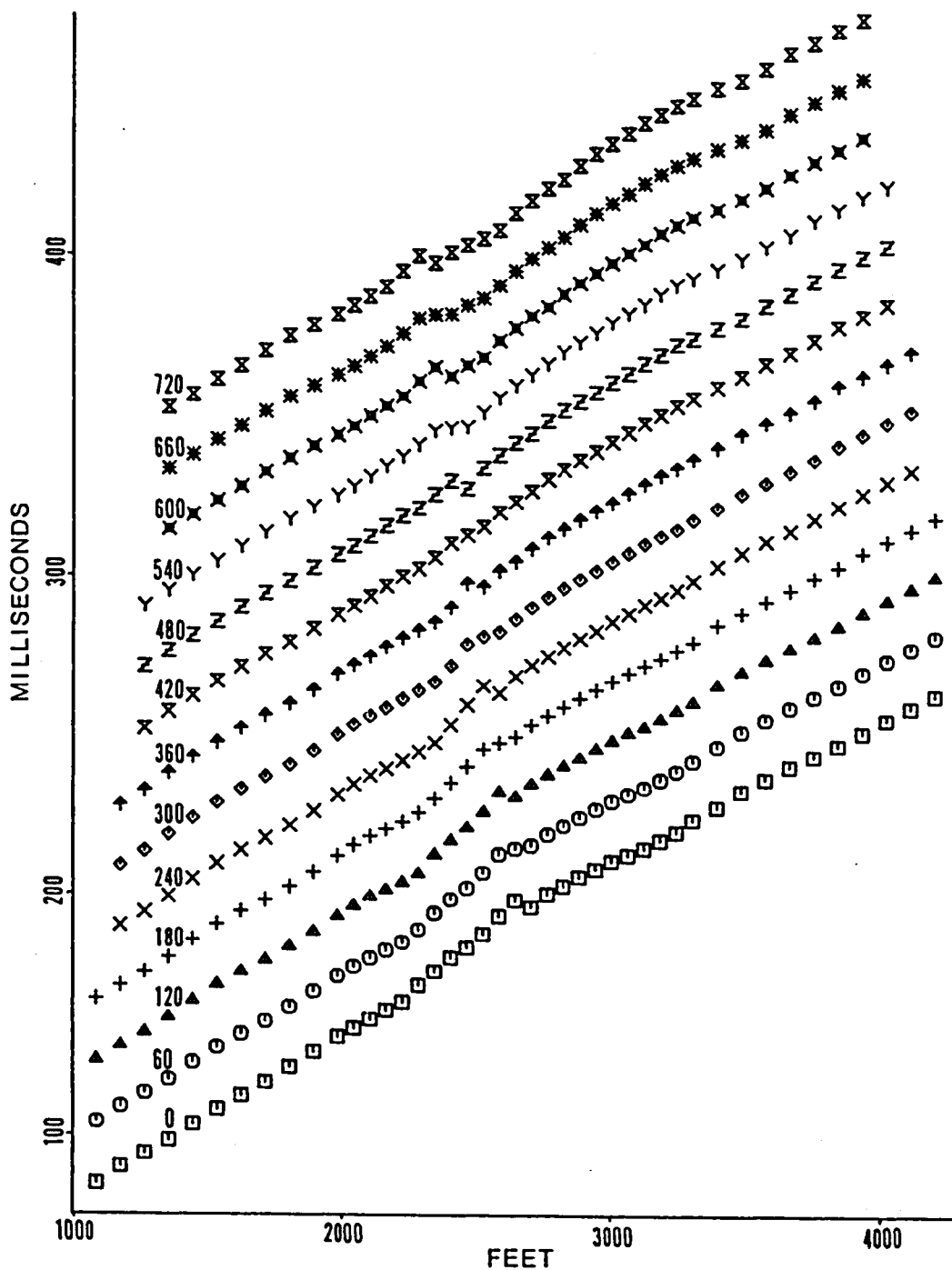


Figure 17. Bedrock velocity analysis curves after removal of shallow anomaly.

10). The curve remains most linear at XY equal to 60 ft. The best determined velocity is still 12,700 ft/s.

#### Conversion of Time-depths to Depth Values

In order to determine depths, a set of time-depths was calculated using the corrected shot-to-shot reciprocal time and the appropriate refractor velocities and XY-values for the three segments of bedrock.

Average overburden velocities were calculated independently over the three segments of the bedrock refractor where XY-values were determined (the fault zone, the upthrown block, and the base of the fault zone on the downthrown block) using equation (4-9). The values obtained, listed in Table 2, agree with one another to within about two percent. Although the optimum XY of 390 ft determined at the base of the fault zone is not well constrained, the near equality of the average velocities obtained over the fault zone and upthrown block, where the refractor velocities contrast most, warrants it reasonable to assume that the average overburden velocity does not vary laterally over the length of the profile. The value of 390 ft gives a consistent overburden velocity term and is therefore considered reasonable. The average velocities derived implies that alluviation over the bedrock pediment surface, in terms of overburden velocity, has not been affected by faulting.

Table 2. Average time-depth  $t_G$ , average overburden velocity  $\bar{V}$ , and depth conversion factor for the three segments of the bedrock refractor.

Location (Geophone Station)	$\bar{t}_G$ (msec)	$\bar{V}$ (ft/s)	Depth Conversion Factor $v \cdot v'_r / \sqrt{v_r'^2 - \bar{V}^2}$ (ft/s)
990-2220	115	4340	4570
2280-2820	110.5	4270	4650
2880-4290	106	4320	4500

Depth conversion factors were calculated for the three segments of the refractor using equation (4-11). The average velocity used in the calculation was the mean of the two values derived where the optimum XY was well determined (i.e., over the fault zone and the upthrown block). The depth conversion factor corrects for the inclination of the emergent critical raypath. The angle of inclination will vary with the velocity contrast between the overburden and refractor. Over those geophone intervals where the refractor velocity was linearly interpolated, the depth conversion factor was independently calculated using the respective refractor velocity. The depth conversion factors are summarized in Table 2. The resultant depth section of the bedrock refractor is illustrated in Figure 18.

The depth section of Figure 18 is the maximum detail bedrock surface that can be determined from the reciprocal composite arrival time curves. Examination of the velocity analysis and time-depth curves has allowed the recognition and successful removal of a near-surface anomaly and the determination of an average overburden velocity to convert time-depths to depth values. In order to infer faulting history from relative displacement of bedrock and subsequent horizons, an attempt was made at mapping shallower alluvial surfaces across the fault.

VERTICAL EXAGGERATION 2X

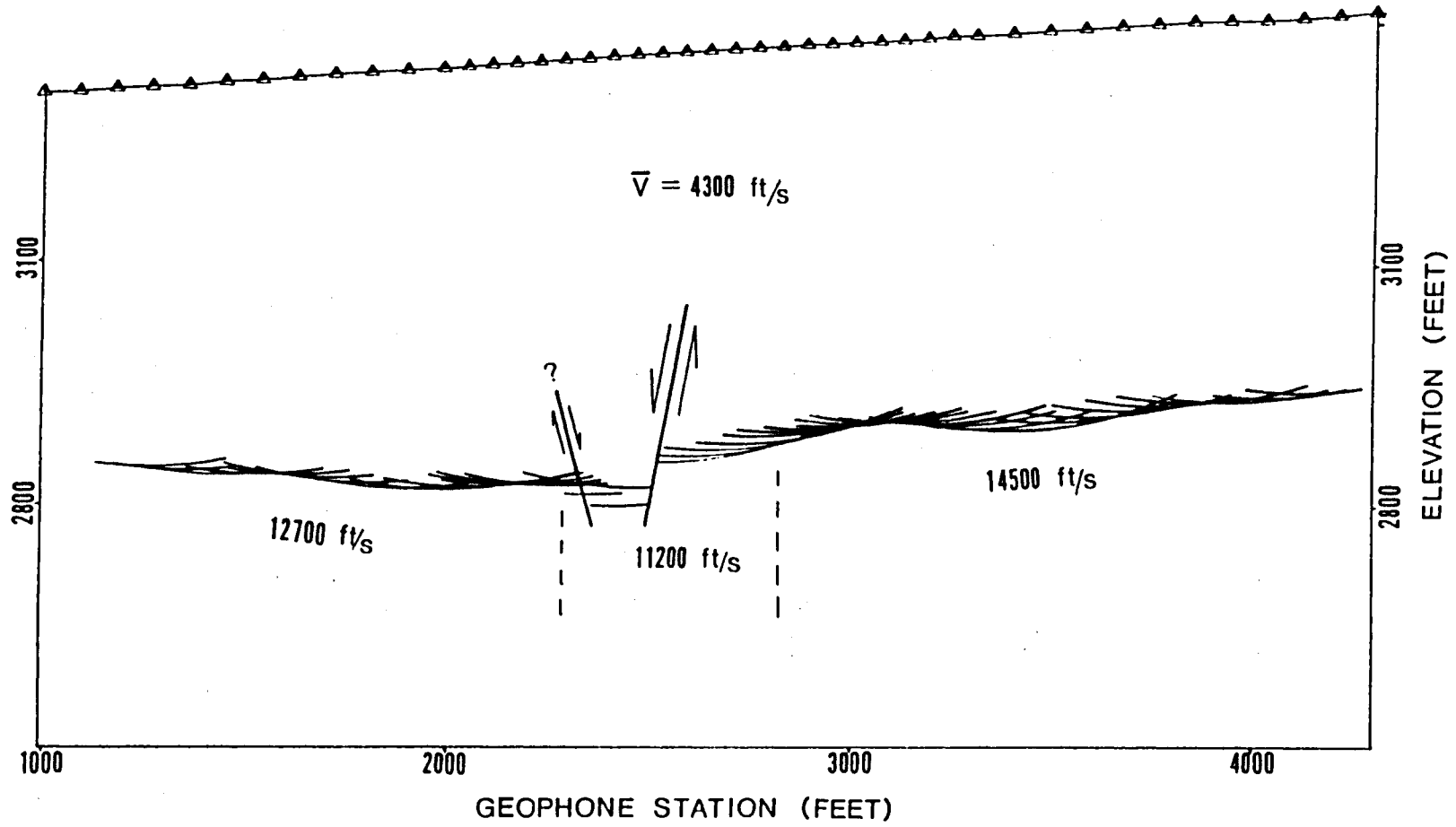


Figure 18. Depth section of the bedrock refractor.

## CHAPTER 5

### MAPPING SHALLOW ALLUVIAL SURFACES

Arrival time data from the base of the LVL occurred extensively enough to map the horizon across the fault. Because of the velocity inversion above this surface, an average overburden velocity had to be derived to convert time-terms separated at geophone stations to depth values.

#### Determining an Average Overburden Velocity for the Base of the LVL

Arrival times corresponding to the base of the LVL are shown in Figure 5. The short, closely spaced reciprocal arrival time data between shots 2 and 2a was collected specifically for this horizon for determination of an average overburden velocity from GRM parameters. The velocity analysis curves of Figure 19 do not clearly indicate an optimum XY-value. The higher time resolution time-depth curves of Figure 20 indicate that the refractor in this vicinity is non-planar. An optimum XY of 80 ft was selected based on delineation of the trough-crest feature extending over the short profile. As stated in Chapter 4, determination of an optimum XY should be based on a refractor feature which extends over several geophone intervals. The trough-crest

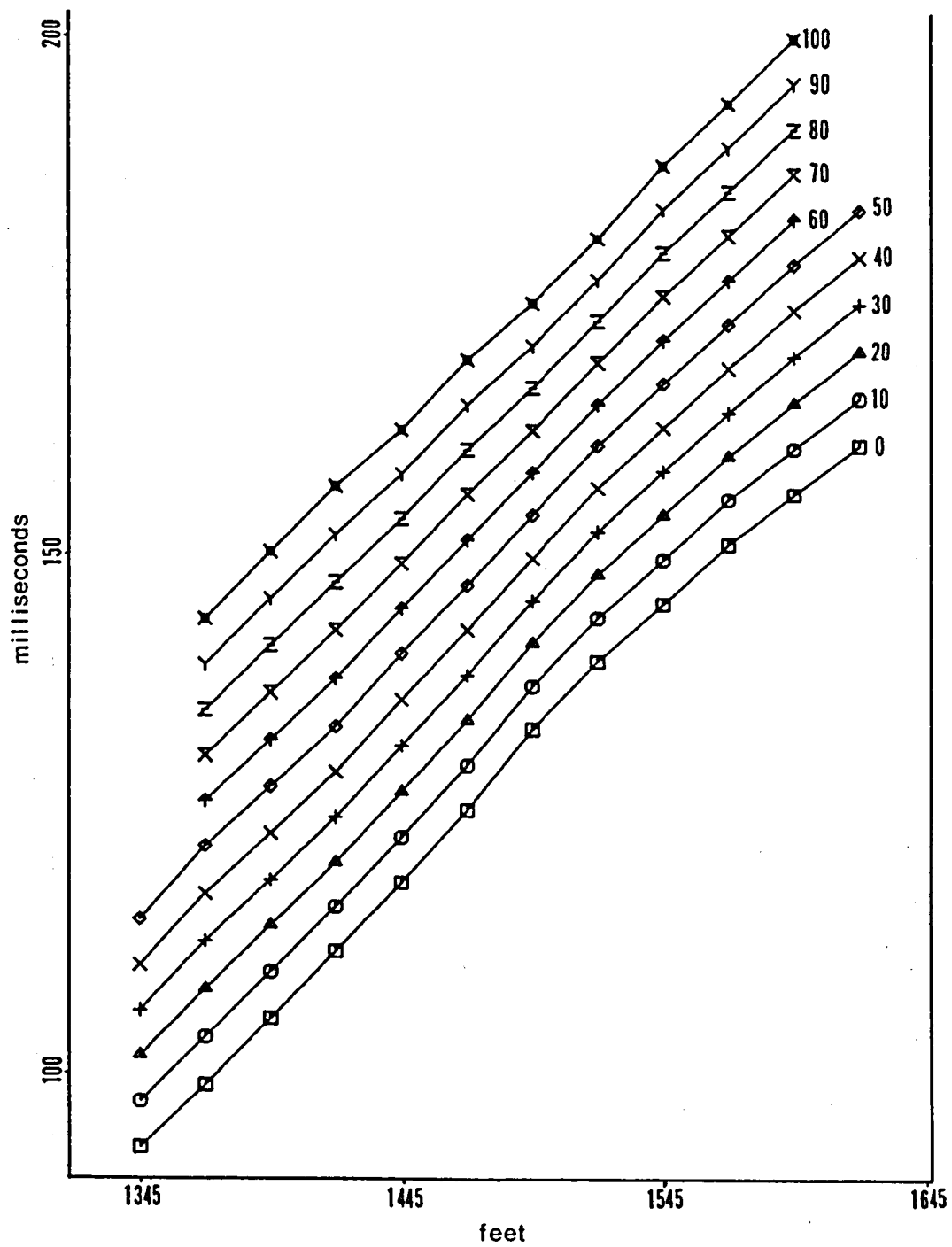


Figure 19. Velocity analysis curves for the base of the LVL.

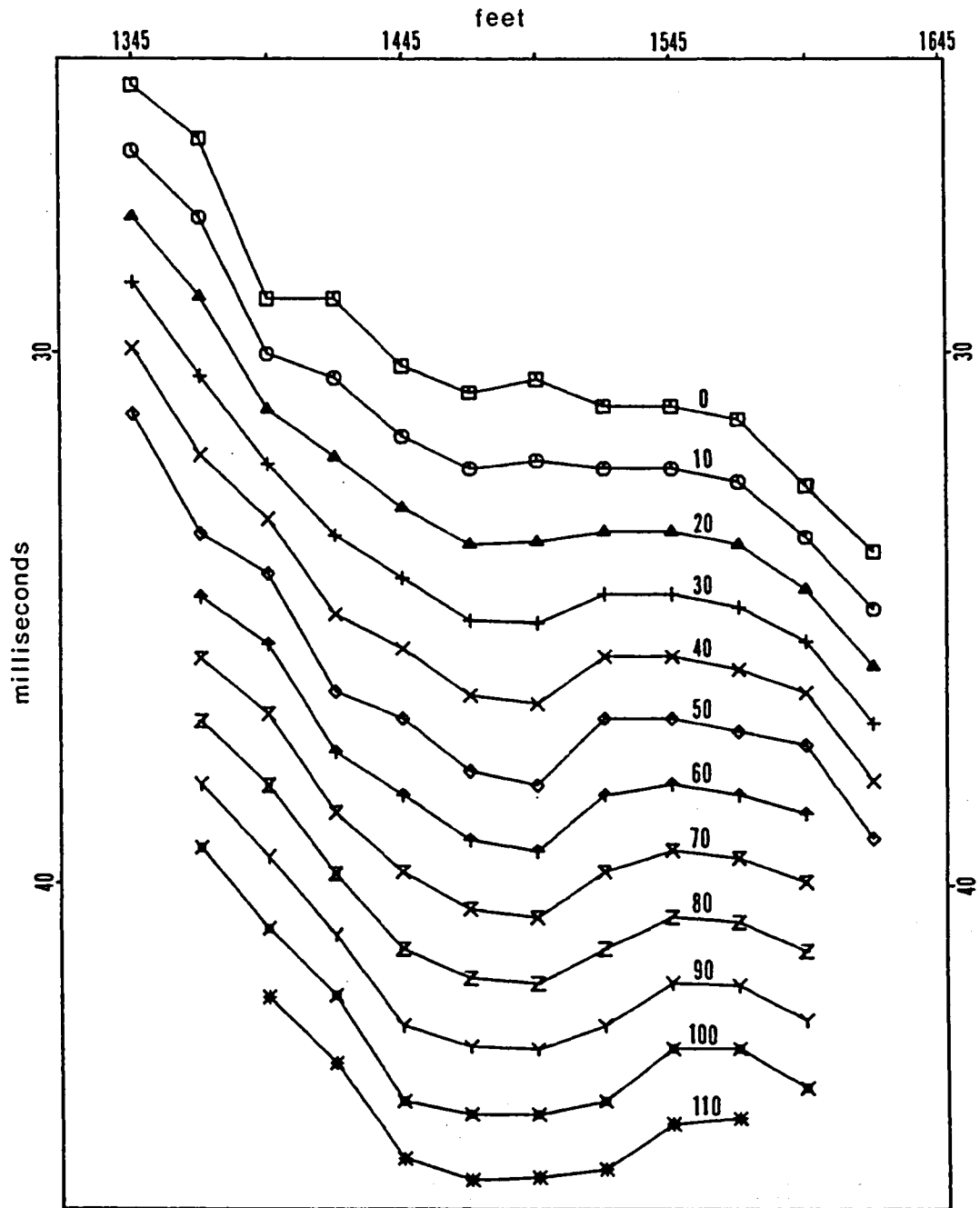


Figure 20. Time-depths for the base of the LVL.

feature defined in Figure 20 is such a feature. The curves are very similar over the range of XY-values 70 to 90 ft, so the median value of 80 ft was chosen. At XY equal to 50 ft, two steps are best defined on the time-depth curves, one between stations 1395 and 1420 and the other between stations 1495 and 1520. These anomalies are only defined over one geophone interval and should therefore not be the basis of choosing an optimum XY-value. The subtlety of the refractor irregularities makes selection of an optimum XY very difficult by inspection of the velocity analysis curves, but a simple comparison of the curves at XY equal to 50 and 80 ft clearly shows that 80 ft gives a better linear fit.

The refractor velocity  $V_r'$  is 4020 ft/s. From the GRM parameters, an average overburden velocity of 2000 ft/s was determined. The depth to the horizon over this 275 ft spread is approximately 70 ft. The results are summarized in Table 3.

Table 3. GRM parameters for the shallow alluvial horizon.

Optimum XY (ft)	$V_r'$ (ft/s)	$\bar{V}$ (ft/s)
80	4020	2000

Mapping the base of the LVL was extended to the fault zone by determining delay times (Gardner, 1939, 1967; Barry, 1967; Wyorbek, 1956) with the arrival time data of shots 2a, 3, and six supplementary, overlapping, unreversed profiles shot in the rangeward direction. The arrival time curves are illustrated in Figure 21.

Determination of the Base of the  
LVL using the Delay Time Method  
of Refractor Mapping

The delay time method is similar to the GRM in that time-terms are separated beneath each geophone station. This term is called the receiver delay time and is by definition identical to the conventional time-depth. The procedure of separating the delay times from the arrival time data is more involved (discussed below) and the restrictive assumptions more limiting. In the normal application of the method, reciprocal delay times corresponding to reciprocal emergent raypaths leaving the refractor at near the same point are migrated to coincide (a step automatically achieved in calculation of the generalized time-depth at the optimum XY) and are then converted to depth values. The shallow refraction data available do not have sufficient reverse common coverage to permit migration. The receiver delay times will instead be treated as time-depths calculated at zero XY, to be converted to depth values as loci with respect to the receiver station at which they are separated.

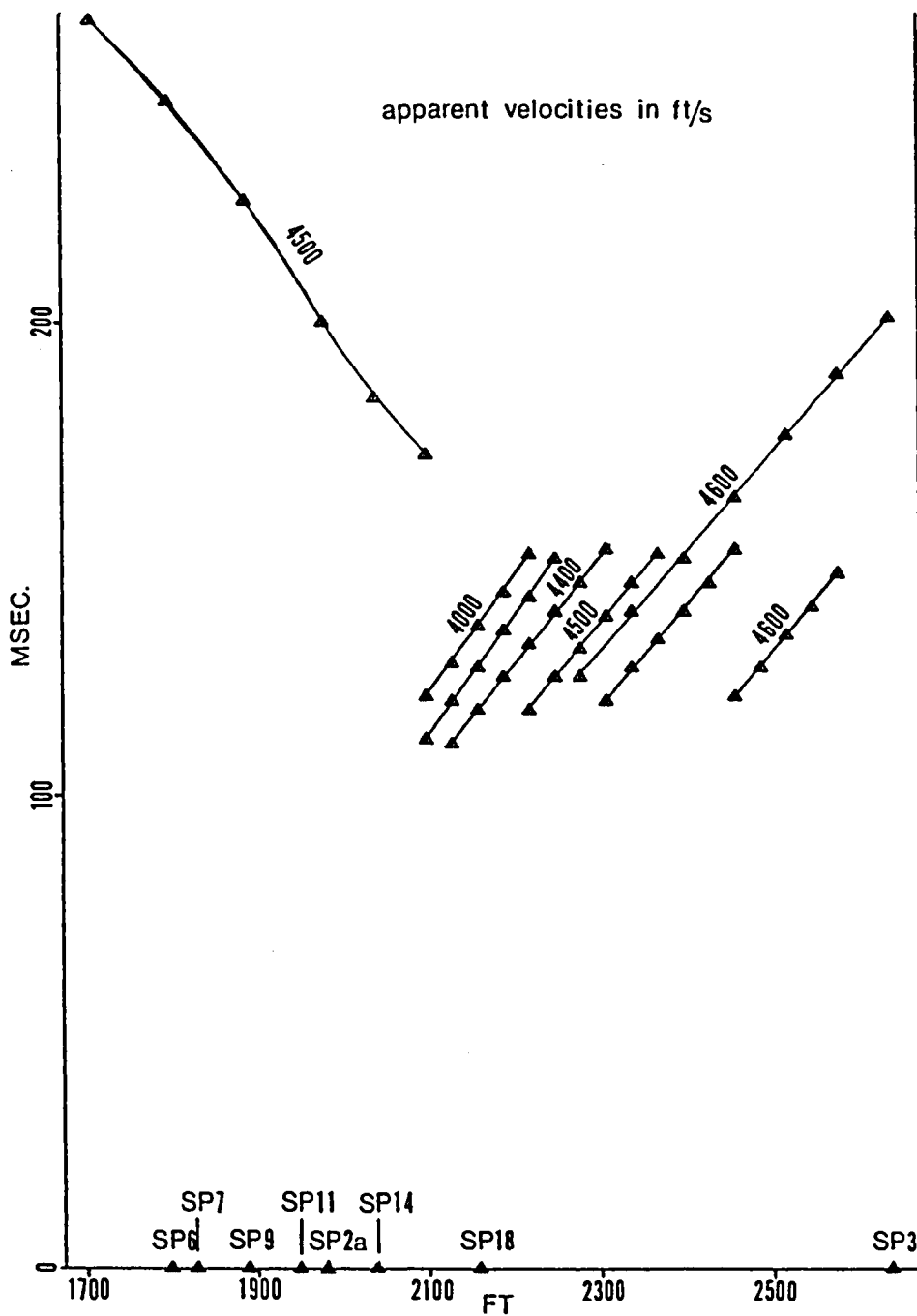


Figure 21. Arrival time data from the base of the LVL of shots 2a, 3 and supplementary shots 6, 7, 9, 11, 14, and 18.

Intercept times (Barry, 1967) were calculated for the six unreversed profiles and shot 2a. The intercept time  $I_{s-r}$ , is defined as the sum of the shot delay time  $\delta_s$ , and the receiver delay time  $\delta_r$ , associated with a shotpoint at  $s$ , and a receiver at  $r$ . The intercept time is calculated at each receiver using the equation

$$I_{s-r} = T_{obs} - x/V_r \quad (5-1)$$

where  $T_{obs}$  is the arrival time at receiver  $r$ ,  $x$  is the offset distance between the shotpoint  $s$  and receiver  $r$ , and  $V_r$  is the refractor velocity. Equation (5-1) is considered a good approximation for the sum of the two delay times,

$$I_{s-r} \approx \delta_s + \delta_r, \quad (5-2)$$

when the dip of the refractor is less than 10 degrees (Barry, 1967).

Figure 22 shows the intercept time curves for the seven overlapping spreads, shot in the rangeward direction, calculated with a refractor velocity of 4600 ft/s. For a gently dipping refractor, the individual intercept time curves for a series of in-line shots should be parallel over the common geophone stations receiving first arrivals from that refractor. The time shift between individual curves will be the difference in the shot delay times,  $\delta_s$ .

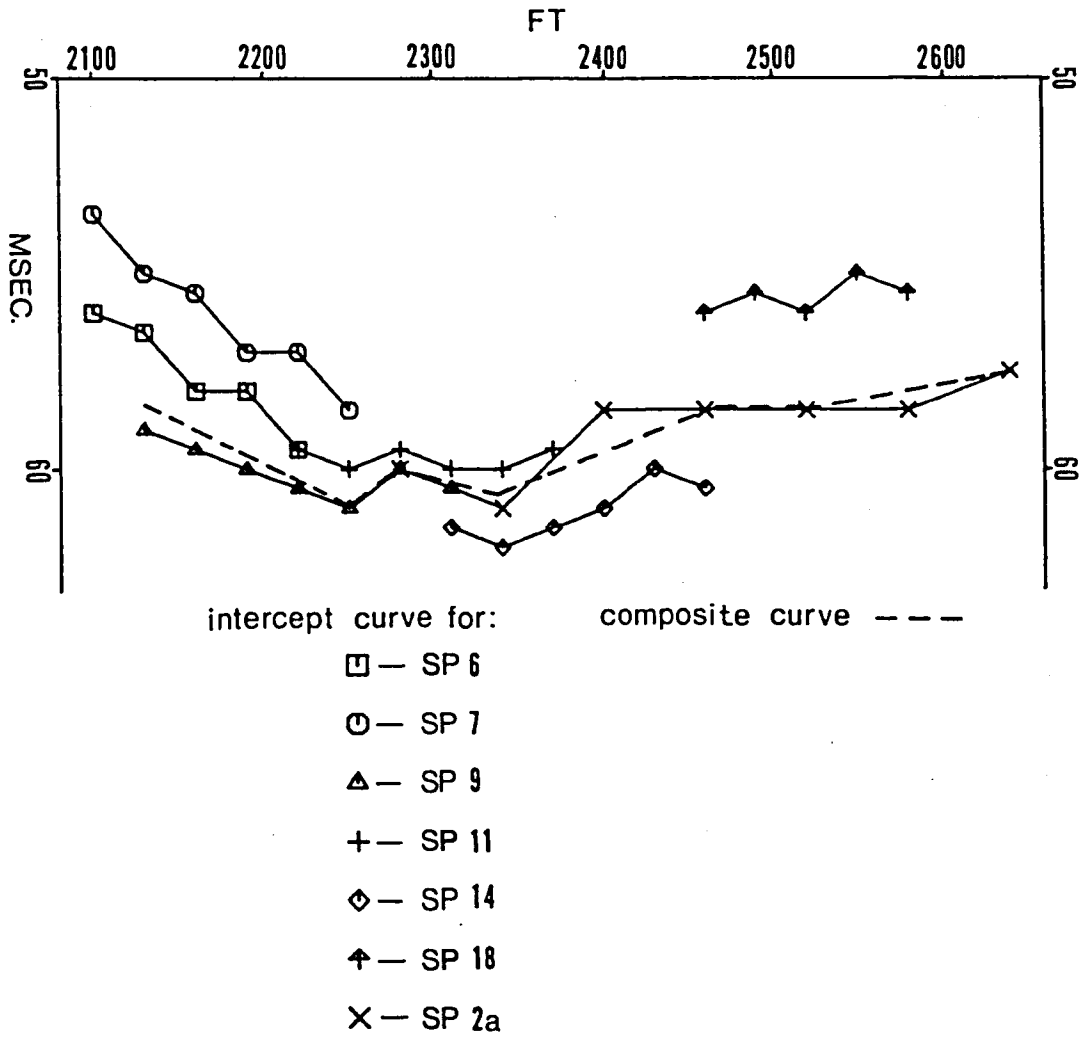


Figure 22. Intercept curves.

A relative intercept time curve was constructed by extending the intercept time curve of shot 9 parallel to the other intercept time curves (Figure 22). This composite curve represents the intercept times which would be calculated if arrival times from shot 9 had been observed from the refractor over the length of the relative curve. The difference of shot delay times for any two profiles can easily be obtained by measuring the time shift  $\Delta T$ , between a relative curve extending through the two respective intercept curves.

The partition of intercept times can be done following the basic method of Barry (1967, pp. 350-351). The shot delay time,  ${}_9\delta_s$ , of shot 9 can be separated from the receiver delay times  ${}_9\delta_r$ , by assuming that the receiver delay time of shot 9 at station 2160,  ${}_9\delta_{2160}$ , is equal to the shot delay time,  ${}_{18}\delta_s$ , of shot 18 (located at 2160). From the relative intercept time curves, the difference in shot delay times is

$$\begin{aligned}\Delta T &= I_{9-r} - I_{18-r} \\ &= {}_9\delta_s - {}_{18}\delta_s,\end{aligned}\tag{5-3}$$

and assuming

$${}_{18}\delta_s = {}_9\delta_{2160},$$

equation (5-3) reduces to

$$\Delta T = {}_9\delta_s - {}_9\delta_{2160} \quad (5-4)$$

Combining equations (5-2) and (5-4), we get

$${}_s\delta_9 = (I_{9-2160} + \Delta T)/2.$$

Knowing the intercept times for shot 9 over the composite curve, the receiver delay times can be obtained at each geophone station by subtracting the shot delay time,  ${}_9\delta_s$ , from the respective intercept time.

In the normal use of the delay time method of refractor mapping, such as Barry's (1967), it is necessary to have common reverse coverage on the refractor in order to determine if the refractor velocity,  $V_r$ , used in calculation of the intercept times, is correct. Relative intercept time curves constructed for both directions of shooting will show the same refractor configuration. Any angular disparity between the two curves, after they are horizontally migrated to coincide, is a measure of the error of the velocity  $V_r$ , used in equation (5-1) (Wyorbek, 1956).

Shot 3 over spreads 1 and 2 is reversed in direction with respect to shot 2a and the six short profiles. The shot delay time of shot 3 to the shallow horizon will be equal to the receiver delay time separated at that location (station 2640) from shot 9. Knowing this, the receiver delay times

can be obtained for shot 3 by subtracting its shot delay time from its intercept times.

Unless the correct refractor velocity  $V_r$  is used in the calculation of intercept times, the partition of shot and receiver delay times will be in error. The delay times of shot 3 have only one common geophone station with the composite values of the forward shots, viz. at station 2100. The receiver delay times at this station should be equivalent for both directions of shooting when the shot and receiver delay times have been correctly separated.

This procedure of separating the delay times was repeated, using different refractor velocities, until the reciprocal delay times at station 2100 coincided. A comparison of the fit for two trial velocities is shown in Figure 23. The refractor velocity of 4600 ft/s is considered best over the interval of stations 1710 to 2640 because at this speed the delay times of shot 3 best fit between the delay times of shot 9 and the time-depths of the short, reciprocated spread from 1370 to 1595 (Figure 23).

The best-determined refractor velocity from the delay time method differs by 600 ft/s from the value independently determined from GRM parameters. This implies a lateral increase in velocity along the shallow horizon going range-ward. It can be seen from Figure 21 that the apparent velocities range from 4000 to 4600 ft/s shooting rangeward. The

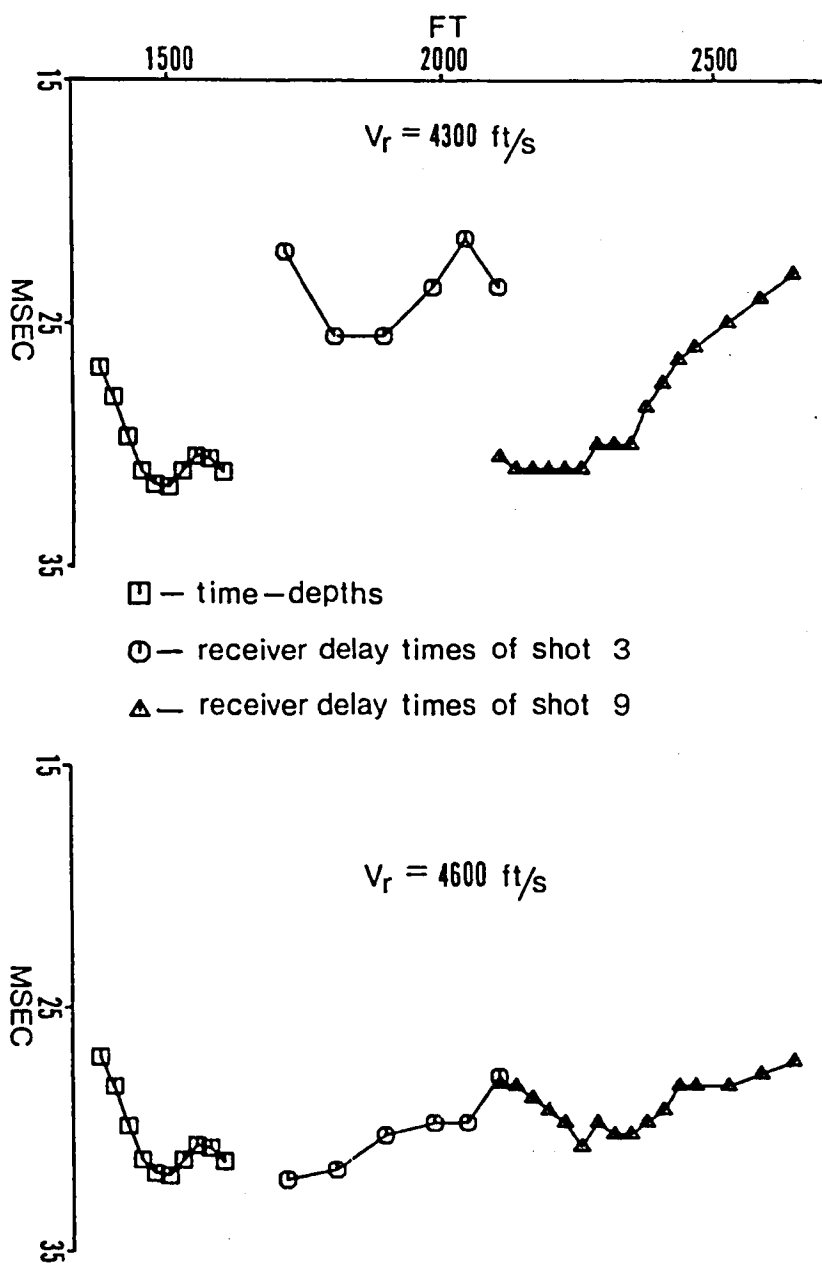


Figure 23. Comparison of fit of delay times.

lateral variation in refractor velocity is probably gradual and the best determined value of 4600 ft/s an average speed over the interval of stations 1710 to 2640.

The delay times were converted to depth values using the average overburden velocity of 2000 ft/s.

Faulting of the shallow alluvial horizon was not directly detected by refractor mapping. A discontinuity of arrivals on the shot records of the rangeward shot 2a though implies a fault. Arrivals from the base of the LVL suddenly cease after stations 2640. Three subsequent traces show very low-amplitude first breaks in a non-linear trend (Figure 5). These arrivals are probably non-critical arrivals from travel paths through the upthrown block of alluvium.

Over the length of spread 3, on the upthrown side of the fault, the base of the LVL has a true velocity of about 3000 ft/s. It is questionable, due to disparity of refractor velocity, whether arrivals following the discontinuities, caused by the high-speed caliche capping lower speed alluvium, are geologically correlated across the fault. Discrete velocity distribution should not be expected for shallow alluvium, and furthermore, the recent faulting may affect differential deposition of alluvium on each side of the fault. Even for a given velocity structure beneath the caliche, variation in the caliche thickness or velocity will affect which travel paths beneath it will arrive as first arrivals.

Determination of an average overburden velocity above the base of the LVL on the upthrown side would be helpful in correlation across the fault. An attempt was made but failed because common coverage of the refractor from reciprocal shots only extended over a few geophone intervals. Regardless, depth values can be assigned over a short interval of spread 3 by converting the time-depths, calculated at zero XY, with the same overburden velocity determined on the downthrown side of the fault.

The depth profile of the shallow horizon is shown in Figure 24. Although the 10 ft of fault displacement determined is not well constrained, the presence of a fault at the location shown is indicated by the discontinuity of arrival times from shot 2a (Figure 5).

#### A Qualitative Discussion on the Deep Alluvial Refractor

On each side of the fault, deeper alluvium is detected from all the shots as first arrivals over a few to several geophone intervals (Figure 5). The apparent velocities measured from these arrival times range from about 5000 to 9200 ft/s. The deep alluvium arrivals from shotpoint 3 shooting rangeward, and from shotpoint 3a shooting basinward, occur more extensively than from other shotpoints and show an increase in apparent velocity with offset (Figure 5). The increase in apparent velocity suggests that a velocity

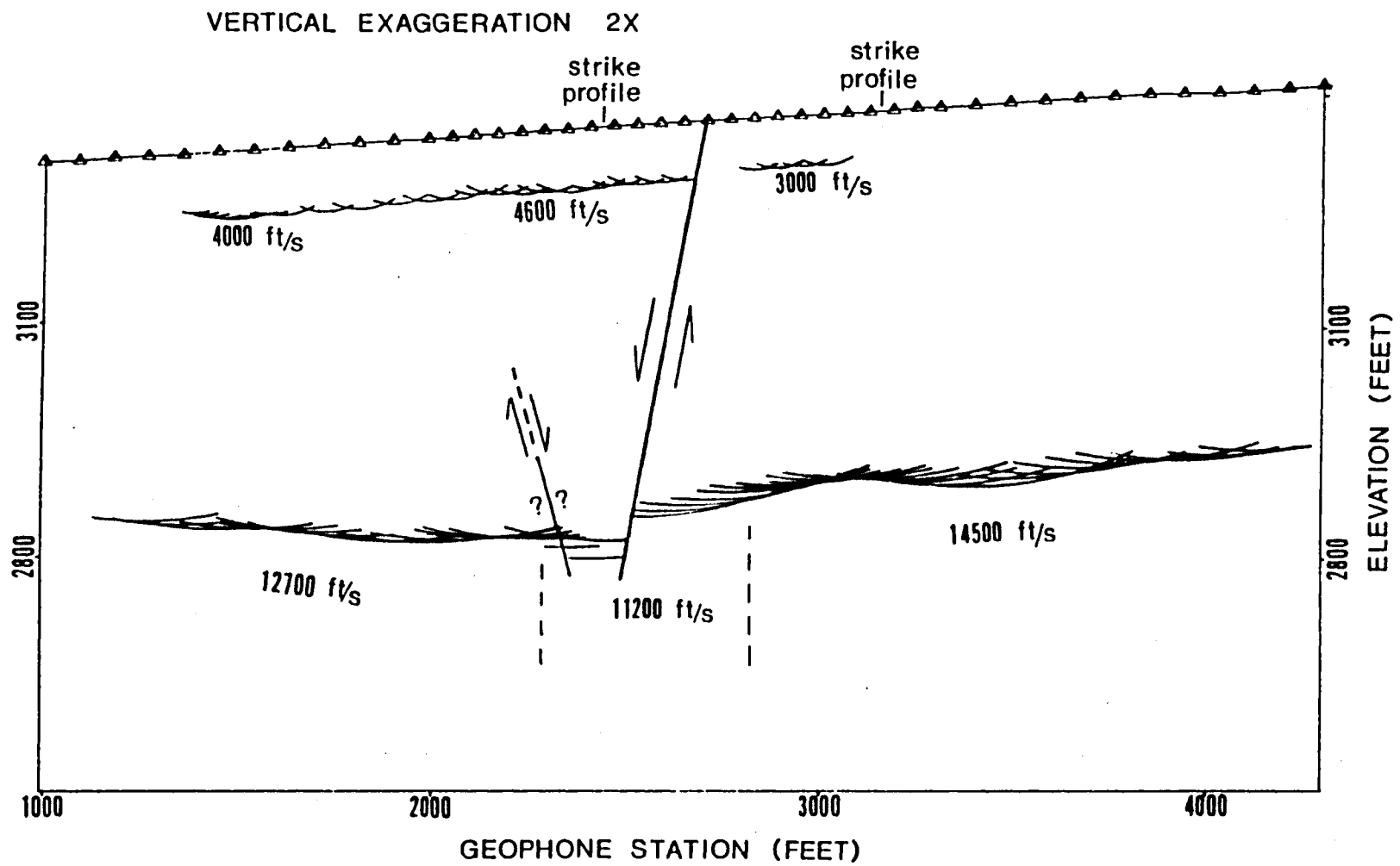


Figure 24. Final dip line depth profile.

gradient exists and that subsequent first arrivals are not the result of a plane wave being generated off a boundary of discrete velocity increase. The lack of any observed arrival time anomaly corresponding to faulting for the deeper alluvial arrivals over spread 2 from shotpoint 3a, where it is expected, further suggests that subsequent first arrivals are the result of progressively deeper and faster travel paths through the alluvium.

The more extensive occurrence of arrivals from the deeper alluvium from shotpoints 3 and 3a may be the result of the base of the LVL being slower over spread 3. This would allow travel paths sampling the upper portions of the deep alluvium to arrive as first breaks. From the other shotpoints, which are located where the base of the LVL has an apparent velocity of about 4500 ft/s, the deep alluvial arrivals occur over about a 180 ft interval. These arrivals do not occur extensively enough to map using advanced methods. The short segments appear linear, but reciprocal segments show large differences in extrapolated reciprocal times. Using simple formulas for plane dipping layers with discrete velocity distributions is therefore not valid. For these reasons, the deeper alluvium was not mapped.

## CHAPTER 6

### INTERPRETATION OF THE STRIKE PROFILES

The first break arrivals of the strike profiles assigned to the bedrock refractor surface were used in tying the strike profiles with the dip profile. The location of intersection of the strike profiles with the dip profile is shown in Figure 24 (for a plan view of the layout, see Figure 2). The arrival time curves for the strike profiles are shown in Figure 25. The dip profile intersects these profiles at their approximate mid-points. In order to tie in the strike profiles with the dip profile, the strike profile arrival times were reduced to the datum elevation of their respective mid-points. The travel time corrections, made for shotpoint and geophone elevation differences with the mid-point of the strike profiles, assumed near-vertical incidence of upward and downward travel paths. No spatial correction for inclination of raypaths was made. The individual trace correction made for each arrival time was the algebraic sum of the difference in elevation of shotpoint and geophone with the datum elevation, divided by a near-surface velocity of 2000 ft/s. The near-surface velocity was

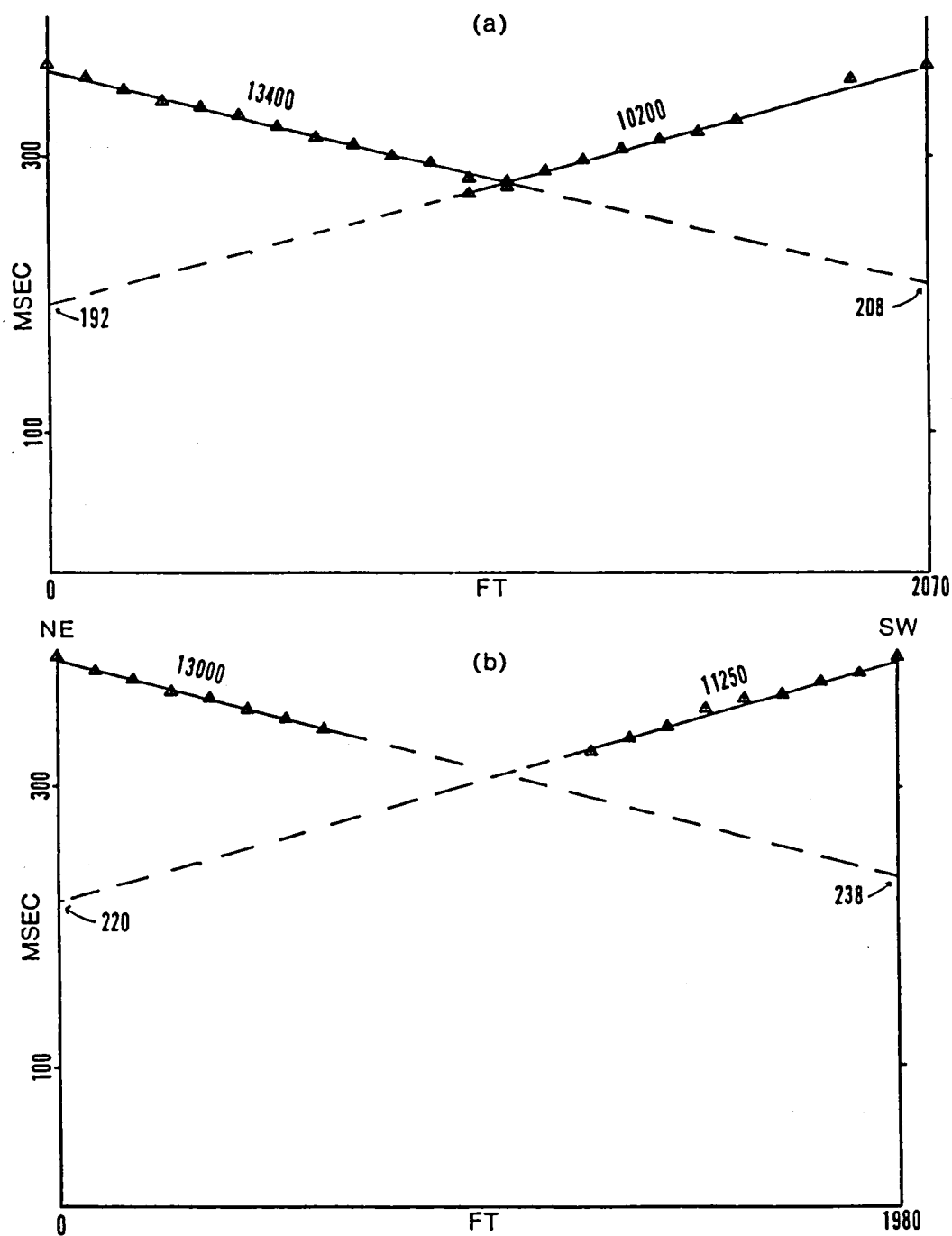
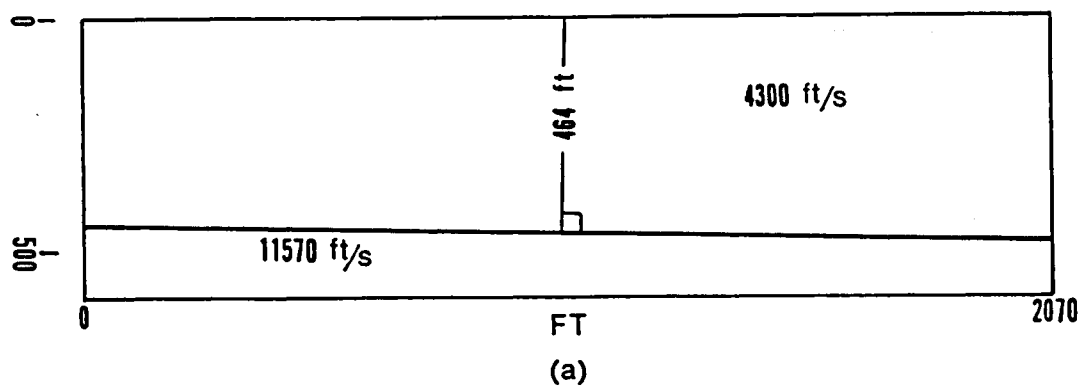


Figure 25. Bedrock arrival time curves of strike profiles. -- (a) Uplithrown; and (b) Downthrown.

determined from short spreads shot on each side of the fault with a geophone interval of 10 ft.

Two depth profiles of the bedrock surface were obtained using the formulas of Mota (1954) for a two-layer case with plane dipping interfaces and constant velocities. The average overburden of 4300 ft/s determined above the bedrock from GRM parameters (Chapter 4) was used as the first layer. The apparent velocities and intercept times for the bedrock refractor were obtained from the least square fit to the data points. The planar bedrock surfaces determined for the strike profiles are illustrated in Figure 26. The interpolated mid-point depths agree quite well with the depths determined at the tie-in points of the dip profile. Table 4 lists and compares the depth values and refractor velocities determined from the strike profile with those determined from the dip profile. On the upthrown side of the fault, the strike profile depth is 10 ft shallower than the dip profile depth, amounting to only a 2 percent difference. The strike profile on the downthrown side of the fault is actually located in the vicinity of the subsurface occurrence of the fault (Figure 24). The dip profile depth value which is compared with the mid-point value of the strike profile in Table 4 is located in a graben-like structure (discussed in Chapter 7). Whether the structure is real and/or extends the length of the strike profile, the dip depth profile of



NE

SW

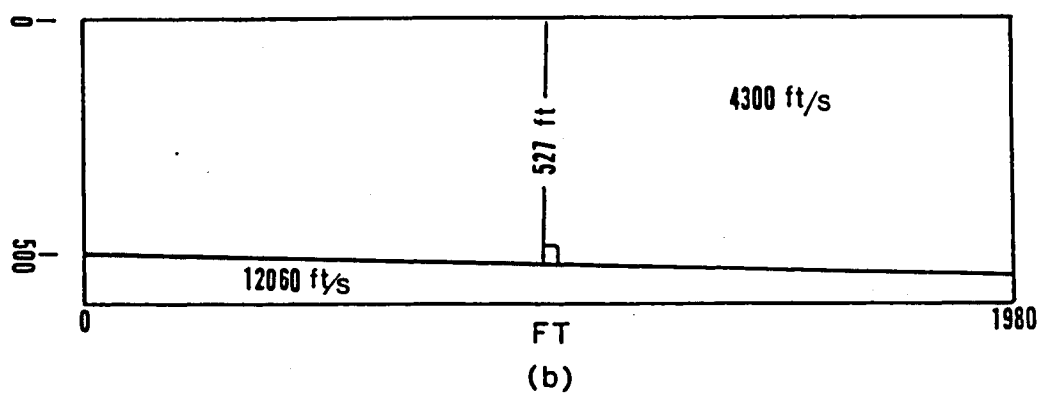


Figure 26. Bedrock depth sections derived from strike profiles. -- (a) Upthrown; and (b) Downthrown.

Table 4. Comparison of depth values and refractor velocity from strike and dip profiles at their respective points of intersection.

	Upthrown Strike Profile	Dip Profile	Downthrown Strike Profile	Dip Profile
Depth (ft)	464	474	527	547
Refractor Velocity (ft/s)	11,570	14,500	12,060	11,200

Figure 24 indicates that travel paths from out of the vertical plane of the strike profile, on each side of the structure, could account for the difference in depth values listed at this location. Regardless, the depth difference is less than 4 percent.

The disparity of refractor velocities is larger than the depth values, especially on the upthrown side of the fault (Table 4). It is assumed in the formulas of Mota (1954) that the refractor velocity is constant along the length of the profile. The difference in ratios of overburden velocity with reciprocal apparent velocities is translated to a dip value and a true refractor velocity. There is no discrimination of lateral change in refractor or overburden velocity with change in dip of the refractor. The GRM, on the other hand, can discriminate between these effects with common

reverse coverage of the refractor. The proven effectiveness of the GRM (Palmer, 1980) indicates that the bedrock refractor velocities determined along the dip profile should be near the true velocities. The inequality of velocities between strike and dip profiles can be explained by the possibility of deviation of subsurface conditions from assumptions made in the derivation of Mota's (1954) formulas. These deviations would be lateral variation in refractor and/or overburden velocity, and lateral changes in refractor dip. The 20 percent bedrock velocity discrepancy on the upthrown side of the fault would require bedrock attitude variations of about 9 degrees along the strike profile. A more reasonable explanation would be lateral variation of refractor velocity along the strike profile due to the strike profile running obliquely to the subsurface strike boundary of the lower velocity fault zone.

## CHAPTER 7

### GEOLOGIC INTERPRETATION

#### Geologic Features

The high-resolution depth profile determined from GRM parameters reveals distinct subsurface geologic features (Figure 24). Extending a line segment through the location of the steps in the bedrock pediment and the shallow alluvial horizon to the surface expression of the fault determines a fault plane in profile dipping about 75 degrees basinward. The undulating, suballuvial bedrock surface, at an approximate depth of 500 ft, shows 50 to 75 ft of offset in the immediate vicinity of the fault. The 25-foot range of offset is given because at the base of the fault some of the depth value as loci do not fall on the envelope of arcs. This implies either a small graben at the base of the fault caused by antithetic faulting or time-depths that are exaggerated by shallow anomalies. If the two deepest depth values are ignored, at stations 2340 and 2400, a continuous refractor surface can be determined to the base of the fault showing an offset of about 50 ft.

The upthrown block of bedrock dips about 2 degrees basinward, parallel to the present-day surface. The down-

thrown block, dipping 4 degrees rangeward, is rotated 6 degrees with respect to the upthrown block.

Ten feet of fault displacement was determined in the shallow alluvial horizon at an approximate depth of 70 ft. Variations of alluviation in time in the local basins of southeastern Arizona since latest Miocene-early Pliocene time are thought to be predominantly climatically induced as opposed to prior tectonic induced fluctuations (Menges and McFadden, 1981). The shallow alluvial horizon is probably such a climatically induced surface, seismically distinguished as a result of variation in the detrital material being transported from the nearby mountains. The poor correlation of velocity across the fault (Chapter 5) may be due to disruption of the alluvial fabric during fault deformation. The apparent velocity observed at the base of the LVL further rangeward, over spread 4, is comparable to that determined on the basin side of the fault (Figure 5).

#### Implications for Faulting History

Relative timing of fault displacement events can be inferred from offset relationships delineated in the subsurface with those observed at the surface. Scarp height in the vicinity of the refraction profile is about 10 to 15 ft. Maximum scarp height observed along the western piedmont of the Santa Rita Mountains was nearly 25 ft. The 10 ft of

offset determined in the shallow horizon is comparable to that observed at the surface. This implies that no faulting has occurred between the time of deposition of the shallow horizon and the earliest faulting recorded at the surface, which is dated at 300,000 to 200,000 years B.P.. The offset delineated in the bedrock pediment surface of 50 ft or more is at least twice the maximum observed at the surface along the Santa Rita Mountains, and at least 3 times that observed in the immediate vicinity of the refraction survey. This indicates some additional displacement, amounting to 40 to 65 ft not recorded by the near-surface horizons, has occurred between the time of burial of the pediment and the deposition of the shallow alluvial horizon.

Faulting prior to development and burial of the bedrock pediment surface can be inferred from the lateral variation in bedrock velocity (Table 1). A high fracture density as a result of fault rupture is probably the cause of the low refractor velocity in the fault zone. The refractor velocity contrast of 1800 ft/s on each side of the fault zone may represent two different lithologies brought to near the same elevation by previous movement along the fault, followed by erosional truncation of the surface.

The occurrence of the sub-pediment, high-speed refractor on the upthrown side of the fault (Chapter 3) also indicates possible movement along the fault prior to burial

of the bedrock pediment surface. The crossover location for the deeper, high-velocity refractor (i.e., where the arrival first occurs spatially) only differs by 90 ft from shotpoints 1 and 2 (Figure 6) even though shotpoint 1 is 990 ft further basinward than shotpoint 2. Shooting basinward, the high-speed refractor is never sampled on the downthrown side of the fault. These two facts suggest that the high-speed refractor is structurally isolated on the upthrown side of the fault, possibly as a result of displacement occurring before the movement recorded in the 50 to 75 ft of offset delineated on the buried erosional bedrock surface.

#### Conclusions

Interpretation of the faulting history from the seismic refraction data is consistent with previous studies. The additional offset delineated in the bedrock surface verifies the inference made in the geomorphic study of Pearthree and Calvo (1982) that late Quaternary faulting events along the Santa Rita Mountains are the result of renewed movement along pre-existing structures. The 40 to 65 ft of additional displacement delineated has been constrained to have occurred over a time span corresponding to deposition of at least 400 ft of alluvium. Tectonic quiescence along the western Santa Rita Mountain front has been estimated to have spanned at least 2 to 4 m.y. before the early Quaternary. These

estimates are based on estimated rates of erosional retreat of the mountain front from the present sites of Quaternary faulting and the degree of erosional embayment of the mountain front. This study has revealed additional displacement having occurred between the inception of pedimentation and the late Quaternary faulting events. The maximum rate of uplift along the western piedmont of the Santa Rita Mountains recorded in late Quaternary alluvial surfaces is about 12 ft per 100,000 years. The additional 40 to 65 ft of displacement constrained to the minimum time period of 2 to 4 m.y. represents relative tectonic quiescence compared to estimates of recent uplift rates. Pre-pedimentation faulting activity is suggested by the refractor velocity contrast across the fault and the apparent structural isolation of the sub-pediment, high-speed refractor on the upthrown side of the fault. Displacement along the fault prior to waning of Basin-Range activity along the Santa Rita Mountains can be inferred from this seismic refraction study but can not be measured because no sub-pediment refractor was detected on the downthrown side of the fault. If the high-speed refractor detected on the upthrown side of the fault has a geologic correlate further basinward, it may be possible to determine the true throw of the fault with a more extensive refraction survey.

## REFERENCES

- Barry, K. M., 1967, Delay time and its application to refraction profile interpretation, in Seismic refraction prospecting: A. W. Musgrave, Ed., SEG, Tulsa, pp. 348-361.
- Domzalski, W., 1956, Some problems of shallow refraction investigations: Geophys. Prosp., v. 4, pp. 140-166.
- Drewes, H., 1973, Structural geology of the Santa Rita Mountains southeast of Tucson, Arizona: U. S. Geological Survey Professional Paper 748, 35 pp.
- Eberly, L. D., and Stanley Jr., T. B., 1978, Cenozoic stratigraphy and geologic history of southwestern Arizona: Geological Society of American Bulletin, v. 89, pp. 921-940.
- Gardner, L. W., 1939, An areal plan of mapping subsurface structure by refraction shooting: Geophysics, v. 4, pp. 247-259.
- Gardner, L. W., 1967, Refraction seismograph profile interpretation, in Seismic refraction prospecting: A. W. Musgrave, Ed., SEG, Tulsa, pp. 338-347.
- Hagedoorn, J. G., 1955, Templates for fitting smooth velocity functions to seismic refraction and reflection data: Geophys. Prosp., v. 3, pp. 325-338.
- Hagedoorn, J. G., 1959, The plus-minus method of interpreting seismic refraction sections: Geophys. Prosp., v. 7, pp. 158-182.
- Hawkins, L. V., 1961, The reciprocal method of routine shallow seismic refraction investigations: Geophysics, v. 26, pp. 806-819.
- Hawkins, L. V., and Maggs, D., 1961, Nomograms for determining maximum errors and limiting conditions in seismic refraction surveys with blind zone problems: Geophys. Prosp., v. 9, pp. 526-532.

- McFadden, L. D., 1978, Soils of the Canada del Oro valley, southern Arizona: M. S. Thesis, University of Arizona, Tucson, 116 pp.
- Menges, C. M., 1981, The Sonoita Creek Basin: Implications for late Cenozoic tectonic evolution of basins and ranges in southeastern Arizona: M. S. Thesis, University of Arizona, Tucson, 239 pp.
- Menges, C. M., and McFadden, L. D., 1981, Evidence for a latest-Miocene to Pliocene transition from Basin-Range tectonic to post-tectonic landscape evolution in southeastern Arizona: Arizona Geological Society Digest, v. 13, pp. 151-160.
- Menges, C. M., Pearthree, P. A., and Calvo, S. S., 1982, Quaternary faulting in southeast Arizona and adjacent Sonora, Mexico: Geological Society of America Abstracts with Programs, v. 14, p. 215.
- Morrison, R. B., Menges, C. M., and Lepley, L. K., 1981, Neotectonic maps of Arizona: Arizona Geological Society Digest, v. 13, pp. 179-183.
- Mota, L., 1954, Determination of dip and depths of geological layers by the seismic refraction method: Geophysics, v. 19, pp. 242-254.
- Palmer, D., 1980, The generalized reciprocal method of seismic refraction interpretation: SEG, Tulsa.
- Pearthree, P. A., and Calvo, S. S., 1982, Late Quaternary faulting west of the Santa Rita Mountains south of Tucson, Arizona: M. S. Prepublication Manuscript, University of Arizona, Tucson, 49 pp.
- Press, F., and Dobrin, M. B., 1956, Seismic wave study over a high-speed surface layer: Geophysics, v. 21, pp. 285-298.
- Press, F., and Ewing, M., 1948, Low speed layer in water covered areas: Geophysics, v. 13, pp. 404-420.
- Scarborough, R. B., and Peirce, H. W., 1978, Late Cenozoic basins of Arizona, in New Mexico Geological Society Guidebook, 29th Field Conference, Land of Cochise: J. F. Callender, J. C. Wilt, R. E. Clemons, Eds., NMGS, pp. 253-259.

- Sene, S., 1983, A shallow seismic reflection experiment in Avra Valley, Pima County, Arizona: M. S. Thesis, University of Arizona, Tucson, 80 pp.
- Shafiqullah, M., Damon, P. E., Lynch, D. J., Kuck, P. H., and Rehrig, W. A., 1978, Mid-Tertiary magmatism in southeastern Arizona, in New Mexico Geological Society Guidebook, 29th Field Conference, Land of Cochise: J. F. Callender, J. C. Wilt, R. E. Clemons, Eds., NMGS, pp. 231-241.
- Stevenson, F., Kretvix, K., O'Connor, L., Calvo, S., Sumner, J., Sbar, M., and Richardson, R., 1981, Report of Geophysical surveys in the Madera Canyon alluvial fan and Arivaca Wash Areas, Pima County, Arizona: U. S. Geological Survey Open-File Report, Tucson.
- Wyorbek, S. M., 1956, Application of delay and intercept times in the interpretation of multilayer refraction time distance curves: Geophys. Prosp., v. 4, pp. 112-130.





3 9001 01952 1858

UNIVERSITY OF ARIZONA LIBRARY

Special  
Collections